LUNDS UNIVERSITET

FASTA TILLSTÅNDETS FYSIK

LUNDS
UNIVERSITET

SPATIALLY RESOLVED PHOTOCURRENT MAPPING OF NANOWIRE ARRAY SOLAR CELLS FOR ANALYSIS OF FACTORS AFFECTING CELL EFFICIENCY

Bachelor's Thesis

Bryan Curtin

21 September 2012

Supervisors: Magnus Borgström & Dan Hessman

1 Abstract

This thesis develops a laser-based technique for spatially resolving the photocurrent from nanowire array solar cells. The technique has been demonstrated to provide information on processing induced defects e.g. poor device contacts, and defects related to the sample e.g. missing nanowires, resolving features down to ~800nm. Moreover, the technique provides information that can be used to relate features to their effect on cell efficiency, and facilitates investigation of the possible mechanisms. An interesting result is that regions with missing nanowires contribute higher photocurrent than the uniform NW array.

The application of the technique realised in this thesis is also found to be limited by various factors. Most notably, noise from the laser and artefacts produced by the electrometer limit the amount of information that can be deduced from the generated current maps. Tilting of the sample and a diffraction-limited spot size with diameter 332.5nm constitute limitations to the resolution of the technique, which was unable to categorically resolve the current from individual nanowires.

2 Acknowledgements

I would especially like to thank my supervisor Magnus Borgström for his guidance and endless patience, his kind manner and openness to questions, and his willingness to invest his time in educating me on the fundamentals of his research. In particular, thank you for energising me with your motivation and desire to realize the potential of NW array solar cells. I am also very grateful for your ongoing commitment and attention to detail when proofreading countless revisions of my thesis, and for tactfully pointing out where I had room to improve.

A special thanks to my co-supervisor Dan Hessman for putting in hours of his own time to guide me through experimental work, providing me with the practical tools and knowledge without which such a project would not have been possible. I now understand that real research involves getting your hands dirty! Thank you for being ready and eager to help whenever I came calling.

Thank you to the postgraduate students who so graciously lent me a hand. In particular, I'd like to thank Jesper Wallentin for teaching me how to bond solar cells with nothing but a few toothpicks and a bottle of silver paste, and Anna Jansson for helping me to become comfortable in the lab by introducing me to the experimental apparatus and for sharing with me her own research.

Cheers to Merlinde Kay, Tomas Brage, Carl-Erik Magnusson, SPREE, and the department of physics & FTF administration for cutting the red tape, and giving me the opportunity to complete my thesis in collaboration with the researchers at Lund University and UNSW.

Last but certainly not least, I'd like to thank my dear friends and family at home and abroad - in Sweden, or wherever you are in the world. Your love and support got me through the tough times. To those who dragged me from the Lund University physics department's computer labs to party in Copenhagen after I missed the only sunny week in the spring of 2012 writing my thesis; to those who made sure I woke up in the morning to continue writing after my first and hopefully last double all-nighter, for cooking my pasta and making me breakfast; and to all the rest of you – you know who you are. Without you, I fear I'd still be hunched over a keyboard in the dark corner of a musty lab somewhere, writing this eternal thesis, and it's fair to say that I would not have had nearly as much fun doing it.

To all who helped me out or simply showed me some kindness during this last year, I feel humbled and privileged to know you. Thank you.

3 Table of Contents

4 Introduction

4.1 Motivation

High-efficiency, low-cost photovoltaics (PV) have been identified as one of the key technologies that will allow us to reduce our carbon emissions and dependence on polluting fossil fuels [1] [2]. Indeed, increasing the amount of energy generated from renewable sources is a necessary objective in order to mitigate the effects of climate change - labelled widely as one of the greatest challenges of the 21st century [1] [3]. Moreover, deployment of renewable energy technologies will provide additional benefits for energy security, energy access, economic and social development, health and the environment, and will improve the quality of life for all from the world's poorest to those in developed countries [1] [3].

The stage is set for this transition. As of 2011, 84% of world net energy consumption was provided by fossil fuels and 11% by hydropower-dominated renewables [4]. But oil and liquid-based fuels are running out, with peak oil variously projected to arrive soon [5] [6]. Amid declining supply in the face of increasing demand for energy, alternative sources must be developed; and quickly, to avoid potentially catastrophic consequences [7].

In stark contrast to the pessimistic energy supply crisis, the sun radiates 3.9×10 6 EJ/year on the earth's sphere, which is 10,000 times the rate of human energy consumption [1]. Photovoltaics in particular possess the ability to directly generate useable electricity from this abundant resource while also providing additional advantages such as no ongoing fuel costs, quiet, pollution-free, low-maintenance operation, and the opportunity for distributed generation - making it a very attractive solution. However, it faces barriers to deployment. While changing government policies are a major obstacle, it is ultimately the *efficiency* and *cost* of the electricity generation technology that will determine its rate of adoption and ability to displace existing generation sources [1] [8] [9].

The extant generation of readily commercialised PV cells is limited by moderate efficiency and high cost owing to high material consumption. Commercialised '1st generation' cells have reached a maximum recorded efficiency of 25%[1] for a single-junction Si cell which represents a 57% improvement from 1983 to 2009 [9]. These cells are now approaching the Shockley-Queisser limit of 31% theoretical maximum efficiency for a single-junction cell based on Si [10]. Thus, there is decreasing room for improving the cost of cells based on this technology.

A '2nd generation' of PV technologies aims to reduce cost at the expense of efficiency by significantly reducing material usage via thin-films [8]. Typical efficiencies for commercial thin film modules settle at around 10 to 11% [1] but cost reductions are already reaching limits imposed by material costs [8].

A more direct approach to achieving high conversion efficiencies involves exploiting the optimized band gaps of III-V semiconductors in multi-junction configurations under concentrated sunlight. A concentrator cell based on a GaInP/GaAs/GaInNAs two-terminal multi-junction device has been recorded with an efficiency of 43.5% [11]. However, this technology is only economically viable for regions with high insolation and the high cost of these cells limits the extent of their application.

Despite rapidly falling prices for solar modules allowing PV to approach grid parity in some markets [12], incremental efficiency improvements will not realize the potential of PV[2] or its wider deployment, and new concepts are aiming to achieve higher efficiencies at lower costs by exploiting advanced concepts in conjunction with low material use [13] [14].

[1] Under standard test conditions at AM1.5 (1000W/m^2) and 25°C

[2] The Carnot Limit for PV energy conversion is 95% [14]

Key research areas in PV surround concepts to both improve efficiency and reduce cost via novel approaches [8] [14]. One approach marked as having potential to generate electricity from light with high efficiency and low cost are PV cells based on nanowires (NWs)[3]. In particular, cells based on either 'forests' or ordered arrays of III-V NWs in multi-junction configurations grown on cheap substrates have the potential to achieve 50% efficiency at low cost, while simultaneously addressing some of the limitations facing current generation PV technology [15].

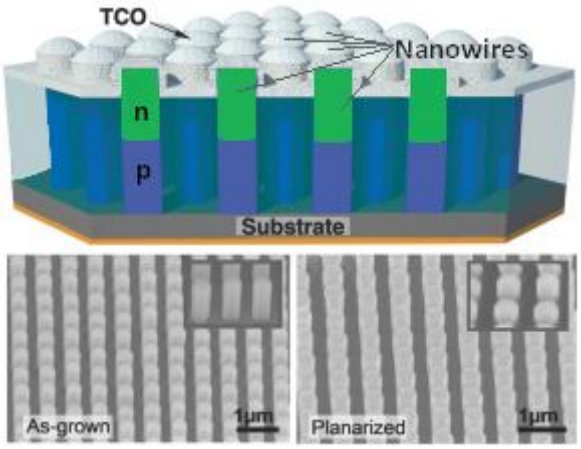

Fig. 1 - Schematic of a NW array solar cell [16][4]

The promise of improving NW array solar cells by developing a technique which enables greater understanding of the factors affecting cell efficiency serves as motivation to this thesis.

4.2 Fundamentals of PV Operation

To understand the operation of a cell based on arrays of NW p-n junctions, it is first essential to understand the operation of the p-n junction – the basis of many electronic devices from diodes & transistors to lasers and solar cells[5].

4.2.1 Doping

Doping is the process of introducing impurities into a semiconductor lattice in order to increase the number of carriers which are free to conduct current. Taking silicon (Si) as a simple example; a lattice of silicon contains Si atoms on the lattice sites with four valence electrons around each atom all participating in covalent bonds. n-type doping involves replacing some of the Si atoms with atoms from a neighbouring group to the right on the periodic table e.g. Phosphorous (P) which has five valence electrons. These atoms provide an additional electron to those required for covalent bonds, and this electron is free to participate in conduction. p-type doping involves substituting some Si atoms with atoms from a group to the left on the periodic table e.g. Boron. These atoms have three valence electrons each, and there is thus an absence of an electron in the lattice created by the introduction of the p-type dopant. This absence is called a 'hole', and can itself be seen as a current carrier. When an electron moves into the space created by the hole, the hole correspondingly moves to the atom from which the electron came, thus acting as a moving charge.

[3] Also known as Nanowires, Nanorods, Nanopillars, Nanocolumns, also Nanospikes
[4] Modified from figure 1 in [16]
[5] See www.pveducation.org/pvcdrom for a description of fundamental solar cell operation

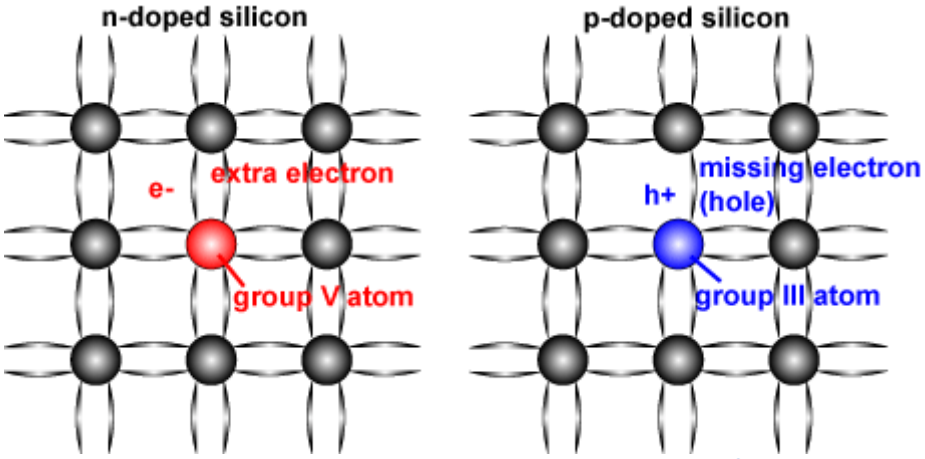

Fig. 2 - Doping a lattice of silicon (PVeducation.org) [17][6]

Thus, an ***n***-type material has extra ***n***egatively-charged carriers (electrons), and a ***p***-type material contains extra ***p***ositively-charged carriers (holes). Doped semiconductors contain more of one carrier than the other, and the carrier with the higher concentration is called the 'majority carrier', while the other is called the 'minority carrier'.

4.2.2 P-n junction

A p-n junction is formed when a positively-doped p-type semiconductor and negatively-doped n-type semiconductor are joined together.

When the p-type and n-type material are joined, the differing concentration of charge carriers in the materials causes the carriers to diffuse across the junction in an attempt to spread out evenly as in frame (1) of Fig. 3. The current caused by this diffusion process is called the diffusion current.

The diffusion of charges across the junction results in a charge imbalance due to the exposed ion cores of dopant atoms that the carriers have left behind. These exposed ion cores set up an electric field in the opposite direction to the diffusion current as in frame (2) of Fig. 3, and this field acts to drive the carriers in the opposite direction by drift transport. The current set up due to this field is known as the drift current.

Under open circuit conditions, when there is no source irradiating the p-n junction, and thus no light-generated current flowing, the opposing drift and diffusion currents reach equilibrium, such that no net current flows.

The drift field between exposed ion cores at the junction accelerates any charges away from the area, and thus results in a zone which is depleted of carriers. This is called the depletion region, and the electric field and corresponding built-in voltage is concentrated here as shown in frame (2) of Fig. 3.

[6] See (2012, S. Bowden & C. Honsberg, http://www.pveducation.org/pvcdrom/p-n junction/doping)

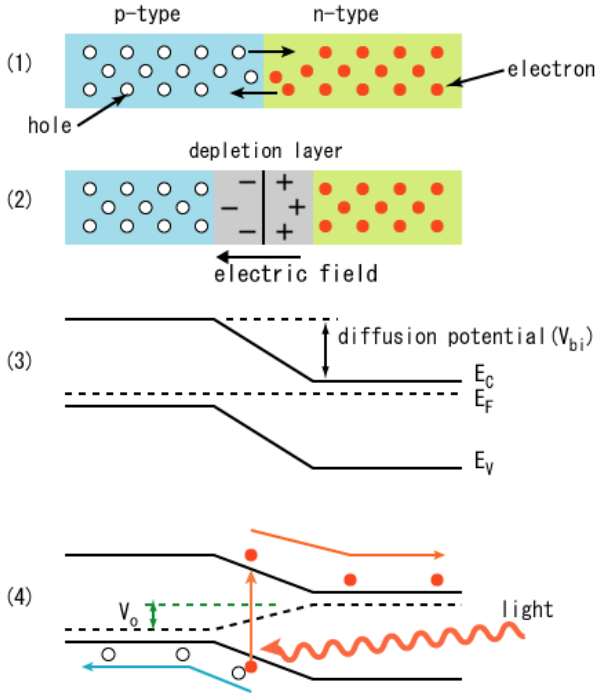

Fig. 3 - Basic operation of the p-n junction (Wikimedia Commons)[7]

The p-n junction can also be described in terms of band structure. In a semiconductor material, there is a gap between the highest available energy state in the valence band, and the lowest available state in the conduction band. For pure, intrinsic semiconductor materials, there exist no states within the band gap that are available for an electron to occupy. Thus an electron can only transition between the highest unoccupied state in the valence band (E_V) and the lowest unoccupied state in the conduction band (E_C). The difference in energy $E_G = E_C - E_V$ is termed the 'band gap energy', and is the energy required for a carrier to be excited from the valence band to the conduction band.

The Fermi level (E_F) is statistically determined to be the energy state with a 50% probability of being occupied by an electron for a solid at a given temperature. For a semiconductor, the Fermi level typically lies within the band gap. However, within the band gap there are never states available for electrons to occupy unless defect (trap) states are present.

Doping introduces extra energy levels just above the valence band for p-type materials, and just below the conduction band for n-type materials. At room temperature, electrons at the donor level in the n-type are given enough energy to become thermally excited (ionized) to the conduction band and act as free carriers. Similarly for p-type materials, holes are ionized from the acceptor level to the valence band where they may participate in conduction. Since the addition of new quantum states near to the band edges results in the ionization of more carriers into the corresponding nearby band, this shifts the Fermi energy towards the band which contains the added majority carriers. This is summarized in Fig. 4

[7] http://commons.wikimedia.org/wiki/File:PnJunction-PV-E.PNG

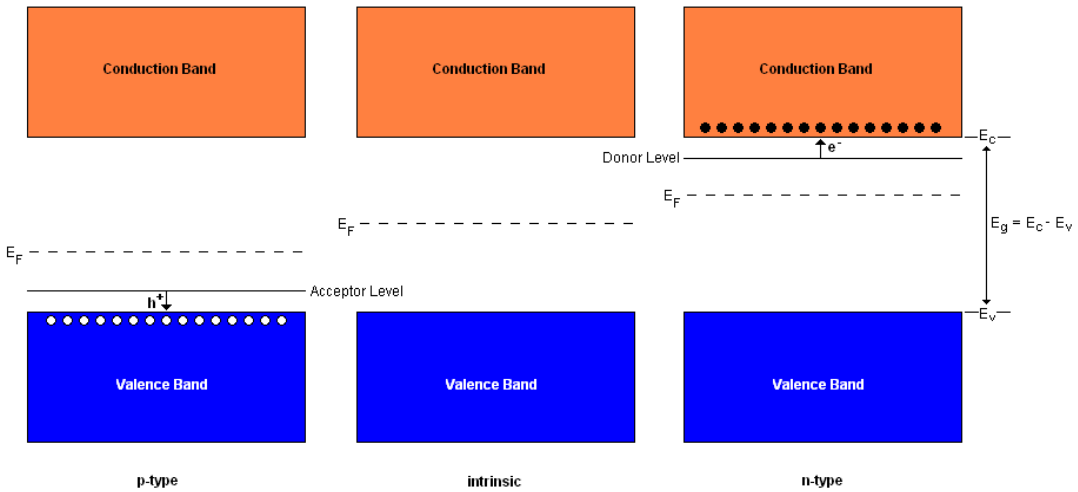

Fig. 4 - Semiconductor band structure indicating band gap and dopant energy levels

When the p-n junction is formed, and the drift and diffusion currents have reached equilibrium, no net current flows. Since the device is in thermal equilibrium, the Fermi level must remain constant throughout the material[8], and since the bandgap is constant for the semiconductor, the bands must bend. Fig. 5 shows the band structure of a p-n junction with the spatial dimension on the horizontal axis.

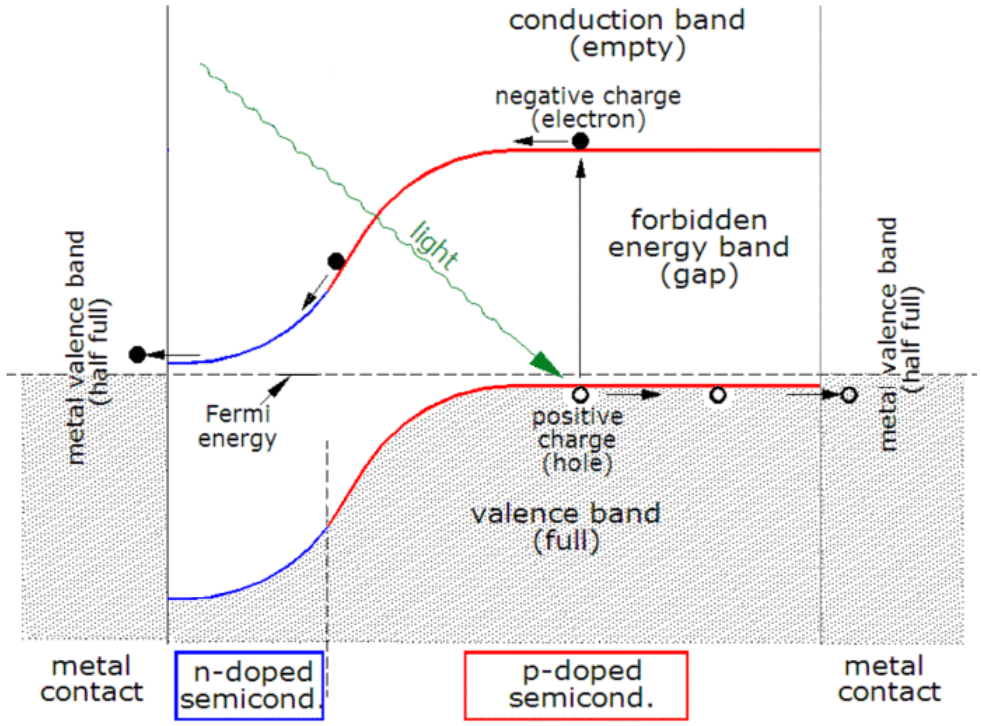

Fig. 5 - Band description of solar cell operation (Wikimedia Commons)[9]

4.2.3 Solar Cell Operation

If a photon of energy equal to or greater than the bandgap energy E_G enters the cell and is absorbed, an electron-hole pair is generated. In other words, both a majority and minority carrier are

[8] Further description at (2012, University of Houston, http://www.ine.uh.edu/research/device-theory/index.php) and (2011, B. Van Zeghbroek, http://ecee.colorado.edu/~bart/book/book/chapter4/ch4_2.htm)

[9] Modified from http://en.wikipedia.org/wiki/File:BandDiagramSolarCell-en.gif

created, and if the minority carrier is within a diffusion length of the junction and manages to reach the drift field across it, it will be swept across the junction at which point it becomes a majority carrier. If the p-type and n-type are connected by a wire, then an electron will move into the external circuit, causing an electron from the circuit to recombine with a hole in the p-type, contributing to the current. This current is the light-generated current or 'photocurrent' (PC).

In terms of the band model of the solar cell, the same process can be described as in Fig. 5. Light absorption of a photon with energy greater than or equal to E_G generates an electron-hole pair, exciting an electron in the p-type to the conduction band. If the electron manages to diffuse to the depletion region, it reduces its potential energy by being swept across the junction (note, holes in the valence band reduce potential energy by 'floating upwards' in Fig. 5), and moves into the external circuit, causing another electron from the external circuit to fill a hole in the p-type.

In order to generate power, however, a solar cell must generate both a current and a voltage. The voltage results from the photovoltaic effect. Under open circuit conditions, for example, light-generated carriers that are collected and separated by the field across the junction result in a build-up of charge that reduces the built-in drift field, setting the p-n junction into forward-bias. This reduced drift field increases the net flow of diffusion current, allowing the charge imbalance to reach a new equilibrium where there is a voltage across the junction. Under open-circuit conditions, this open-circuit voltage (V_{OC}) is equal to the maximum voltage that the cell can produce – it is the voltage required to produce flat band conditions.

In the dark, a solar cell behaves like a diode. When light shines on the cell, however, the light-generated current is superimposed over the current given by the current-voltage (IV) characteristics of the cell in the dark. The solar cell IV-curve is given in Fig. 6 below.

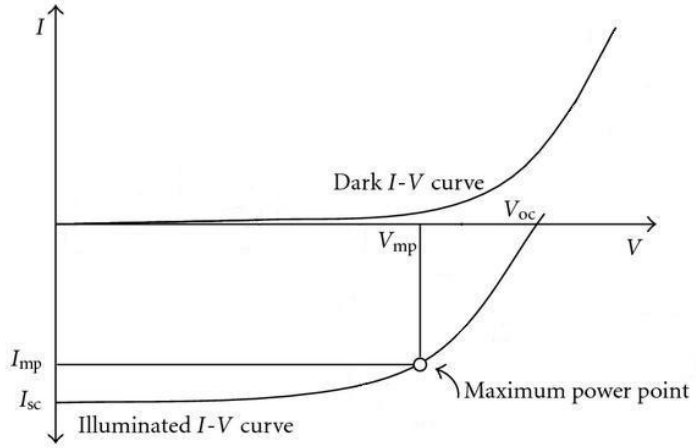

Fig. 6 - Solar cell IV curve

The IV Curve shows that when in forward-bias, the solar cell exhibits a diode current-voltage response, with the current simply shifted due to the presence of a light-generated current.

Since the power generated by the solar cell is given by $P = IV$; the IV characteristic shows that at short-circuit conditions, the solar cell produces its maximum current, but develops no voltage, and thus no power. At open-circuit conditions, the cell produces maximum voltage, but once again no power because no current flows. At any point in between these two conditions I_{SC} and V_{OC}, the solar cell behaves as a forward-biased diode, and by biasing the cell, one can set the current-voltage relationship such that the cell is producing maximum power. This is the basis of using the p-n junction to produce photovoltaic power.

4.3 Nanowires

There are varying definitions of the term 'nanowire', but for the purpose of this document, at least, "Nanowires are one-dimensional, anisotropic structures, small in diameter, and large in surface-to-volume ratio" [18]. In particular, a semiconductor NW is a NW composed of semiconducting material.

4.3.1 Nanowire Synthesis

There are two main approaches to NW synthesis, which can be categorised as either top-down or bottom-up processes. The top-down approach involves breaking up a larger piece of material into NWs, whereas a bottom-up approach involves the formation of NWs from their constituent adatoms. The bottom-up approach is more common.

The Vapor-Liquid-Solid method (VLS) is a common bottom-up method for synthesizing NWs [19]. In this method, a metal seed particle – a liquid alloy catalyst – is first deposited on the growth substrate. The source material for the NWs is then introduced in the gas phase, adsorbing to the liquid catalyst surface, from which the crystal source material diffuses into the liquid droplet until it reaches the point of saturation. Further adsorption of the source material supersaturates the liquid alloy which then nucleates a solid precipitate underneath the metal seed particle. The solid precipitate then becomes the preferred nucleation site for the source material, and the further deposition of material results in the anisotropic growth of a whisker[10] or NW with diameter dictated by the size of the droplet [18]. The seed particle rides on top of the growing NW and ultimately remains on top of it.

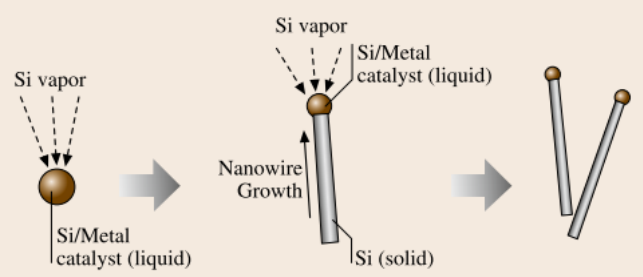

Fig. 7 - Schematic for VLS growth of a silicon NW [18]

NB: there is some disagreement over whether the above growth mechanism is facilitated by a liquid seed particle, or in fact, whether it occurs by diffusion through a seed particle in the solid phase. See [20] [21] [22] [23] for more details.

NWs grown by the VLS method are often fabricated by Metal Organic Vapor Phase Epitaxy (MOVPE)[11]. This process involves introducing the source material as organic compounds or metalorganic compounds (as 'precursors') in the vapour phase. The compounds undergo a reaction, whereby the metalorganic compounds pyrolize (decompose due to high temperature) at the growth surface, depositing the desired metallic source material while the organic by-products leave the reactor. An example of the process not in conjunction with VLS growth of NWs is given in Fig. 8 below.

[10] 'whisker' is a term from older literature on small structures and describes micrometer-thick wires
[11] Also known as Metal Organic Chemical Vapor Deposition (MOCVD)

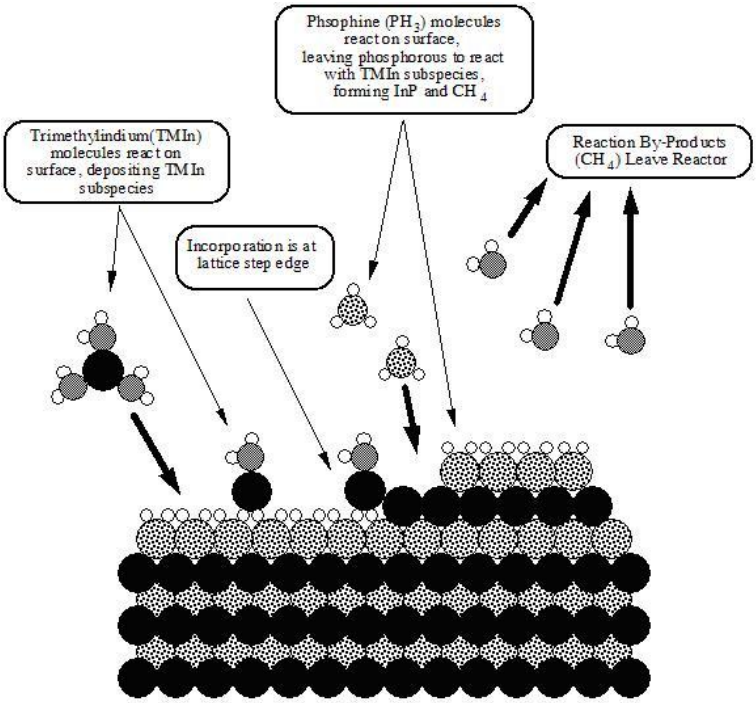

Fig. 8 - An example of the MOVPE process (Wikimedia Commons)[12]

4.4 NW PV

There have been many papers written on the formation of p-n junctions in single NWs for photovoltaic applications [24]. Each NW is grown with differently doped regions so that it contains a p-n junction. These p-n junctions can be formed within the NW in either a core-shell or axial configuration.

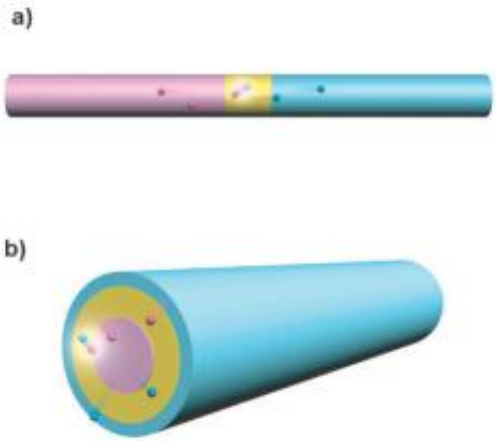

Fig. 9 - Axial (a) and Core-Shell (b) NW p-i-n junctions [25]

In Fig. 9, the pink, yellow and blue sections represent p-type, intrinsic and n-type semiconductors respectively. Pink and blue spheres represent holes and electrons respectively. The single p-i-n NWs behave analogously to p-n junctions occurring in regular solar cells [25].

In a NW array solar cell, a large number of these NW p-n junctions are grown in a forest or array configuration on a substrate and each NW operates as an independent solar cell, generating current which contributes to the total array current, as confirmed in [16] and [26].

[12] http://en.wikipedia.org/wiki/Metalorganic_vapour_phase_epitaxy

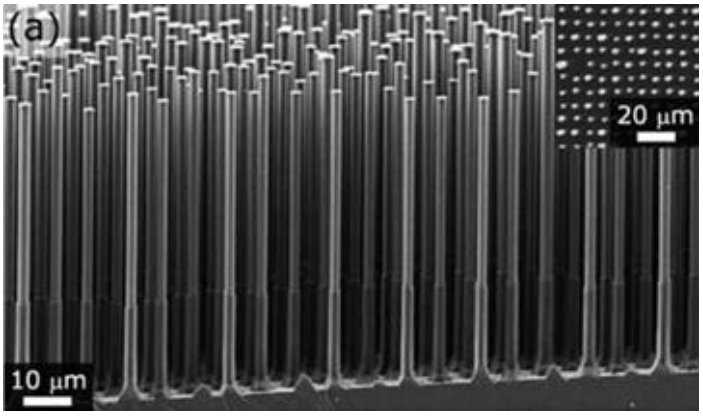

Fig. 10 - SEM image of a silicon microwire array after p-n junction formation[13]

Cells based on NW arrays hold numerous advantages over conventional cells [15]:

- They exhibit high optical absorption despite low volume fill factors, reducing material consumption
- NWs accommodate strain via radial expansion or contraction, thus allowing for previously unattainable material combinations to be realized in axial NW heterostructures, making possible ideal bandgap combinations for multi-junction cells
- Possibility for radial p-n junctions in NWs allowing low diffusion lengths for carrier collection but long photon absorption lengths

There are as yet few research groups capable of realizing fully functional NW array solar cells [15] [27]. Thus far, efficiency figures of up to 7.9% have been reported [15] [26], and research in the field is advancing swiftly [28]. The group at Lund University where this thesis is conducted is aiming towards high efficiency tandem multi-junction concentrator cells based on arrays of III-V axial NW p-n junction heterostructures linked together by Esaki diodes, grown on cheap silicon substrates [15].

This concludes the description and basic function of an NW array solar cell[14].

4.5 The Sample NW Array Device & Fabrication

The sample mapped in this thesis is a NW array solar cell composed of highly ordered axial indium phosphide (InP) p-i-n junctions on an InP(111)B substrate. The sample was grown via MOVPE by the VLS method with an Au metal seed particle as described in [15] and [29].

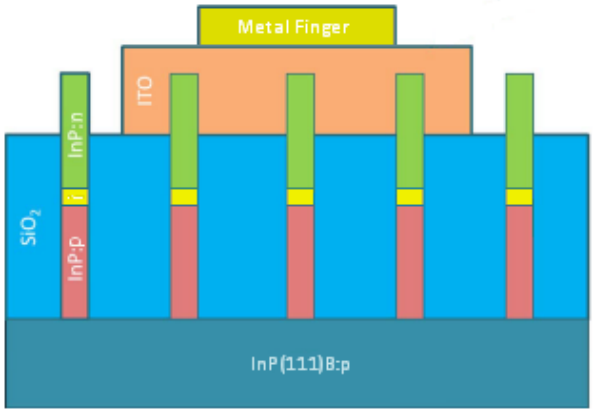

Fig. 11 - Schematic of the sample device [15]

[13] Modified image from [26]
[14] See [28] for a review of Nanowire Solar Cells

Processing stages:

1. A highly-doped p-type InP substrate grown by the Czochralski process is patterned via nano-imprint lithography to define a highly uniform array of Au growth sites for InP NWs. The lithography process is described in [30]
2. InP NWs are grown via MOVPE by the VLS method using trimethylindium (TMI) and phosphine (PH_3) as the precursors which pyrolize to form the InP NWs. Diethylzinc (DEZn) is used as a p-type dopant precursor, which dopes the NW to p-type *in-situ*. The process incorporates *in-situ* HCl etching to prevent radial growth
3. A section of intrinsic InP is grown on top of the p-type NW
4. The final n-type section of nanowire is grown, using tetraethyltin (TESn) as the n-type dopant precursor
5. The Au seed particle is removed from the wire tips
6. The array is coated in an SiO_2 dielectric to embed and isolate NWs
7. NW tips are exposed via etching and contacted via deposition of an ITO (Indium Tin Oxide) transparent conducting oxide layer
8. Metal busbars and fingers are defined by lithography and metal evaporation[16]

An SEM image of the sample follows in Fig. 12, revealing the highly ordered and uniform NW array.

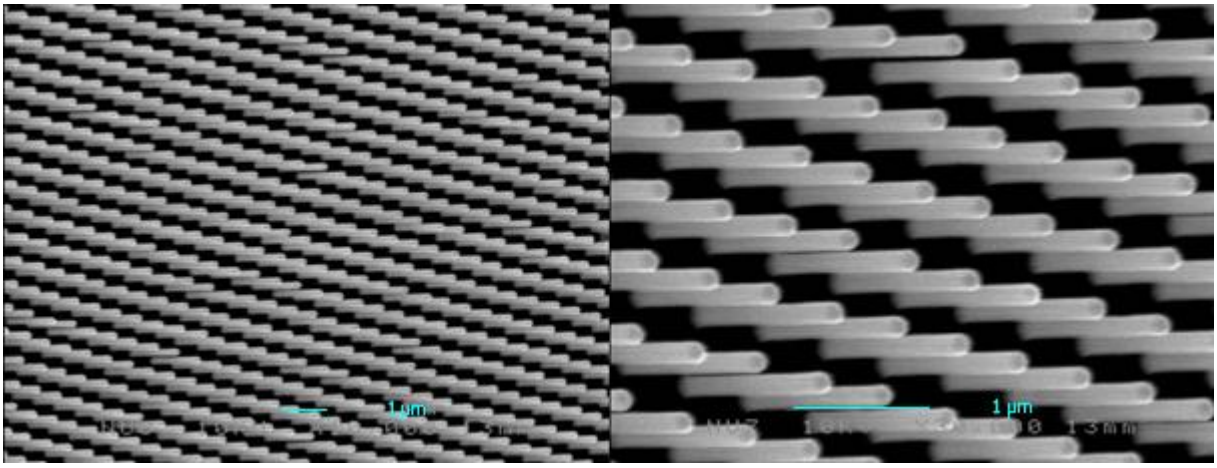

Fig. 12 - SEM image of the sample NW array[17]

The final device consists of several 1mm x 1mm highly ordered arrays of InP nanowires on p-type InP substrates. Each NW is 2µm long, 130nm in diameter, and NWs are spaced with a 500nm pitch (the shortest distance between two adjacent NWs).

Each InP NW consists of an axial p-i-n junction, which operates in the same manner as a p-n junction, excepting the addition of an intrinsic layer between the p-type and n-type which serves to increase the width of the depletion region. This increases the charge separation – with a larger depletion region, more electron-hole pairs are excited in the region with the built-in electric field – and thus increases internal quantum efficiency (IQE)[18], resulting in a higher light-generated current.

The device was characterized, with reported V_{OC} = 0.33V and I_{SC} = 0.06A with an efficiency of 1%. On account of the low efficiency one can assume the Au seed particles have been left on top of the

[15] Modified image from [15] using data provided in email communication
[16] ITO has a large sheet resistivity, so metal contacts are used to extract carriers
[17] Note: scale bars only refer to the 2D plane normal to the SEM and thus only serve to roughly indicate scale
[18] The ratio of carriers collected to the amount of photons absorbed in the device

NWs. Note, the low V_{OC} indicates short-circuited NWs. Hence, this sample is well-suited to this thesis, as the deficiencies warrant further investigation by the development of a PC scanning technique.

4.6 Spatially-Resolved Photocurrent

As discussed in section 4.2.3, photocurrent is the current produced when light-generated carriers are collected by the p-n junction. This current can be measured when the cell is contacted, and the current reading serves to provide information on the solar cell's operating characteristics.

The basic operating principle of PC measurements is described here. The IV Characteristic of the solar cell is given by the Diode Equation with an extra term to indicate the shift of the curve in the current axis, due to the light-generated current, I_L.[19] See Fig. 6 for the corresponding IV Curve.

$$I = I_0 \left[\exp\left(\frac{qV}{nkT}\right) - 1\right] - I_L$$

Often, the equation and corresponding curve is flipped in the current axis, in order to demonstrate that the solar cell is acting as a current source. In any case, it is important to note that at short-circuit conditions, with V=0 (no biasing), the magnitude of the current I_{SC} is simply equal to the magnitude of the light-generated current I_L.

The area-independent short-circuit current[20] of the cell can be approximated by [17]:

$$J_{SC} = qG(L_n + L_p)$$

Where

- G is the Generation Rate
- L_n and L_p are the electron and hole diffusion lengths, respectively

The Generation rate is given by[21]:

$$G = \alpha N_0 e^{-\alpha x}$$

Where

- N_0 = photon flux at the surface (photons/unit-area/sec.)
- α = absorption coefficient
- x = distance into the material

Combining the equations, one can determine an expression for the current density due to an irradiation source of given irradiance H in W/m^2 (the power per area of the incoming beam).

$$J = J_{SC} = J_L = N_0 . q\left(L_n + L_p\right) \int_0^x \alpha e^{-\alpha x}\, dx$$

It is thus clear that the measured current varies in proportion with the photon flux, which is proportional to the irradiance. In other terms:

$$\mathrm{J_{SC}} \propto H$$

This is the basis for spatially-resolved PC measurements.

[19] (2012, S. Bowden & C. Honsberg, http://www.pveducation.org/pvcdrom/solar-cell-operation/iv-curve)
[20] (2012, S. Bowden & C. Honsberg, http://www.pveducation.org/pvcdrom/solar-cell-operation/short-circuit-current)
[21] (2012, S. Bowden & C. Honsberg, http://www.pveducation.org/pvcdrom/p-n junction/generation-rate)

How is it that a spatially-resolved PC reading can provide useful information on cell operation? Since $J_{SC} \propto H$ for the p-n junction, then assuming one irradiates a cell with a beam of constant irradiance; moving over the cell, one would expect to read a spatially uniform current. Any deviations from a uniform current reading would indicate one of two things:

- The region being irradiated is not behaving like the expected p-n junction, and thus there are local variations in electrical properties for example series resistance, recombination velocity, short circuits, faulty contacts. In the case of NW arrays, this could indicate NWs or groups of NWs with different electrical properties, poorly contacted NWs, short circuits (one of which can limit the output of an entire array of NWs) or even the lack of a NW p-n junction (broken NWs).
- The radiation is subject to other localised effects which alter the beam's power density before collection in a p-n junction. For example, scattering or concentration of the beam, shadowing by opaque objects such as metal contacts, absorption in the ITO layer covering the NWs.

Thus, PC measurements are useful for providing information about device characteristics, and they establish the link between those characteristics and the current output which is ultimately a key metric of interest in a solar cell designed for power generation. In particular, spatially-resolved PC can be combined with other spatially-resolved information on cell characteristics (e.g. topograms, camera images), allowing one to understand the relationship between the resultant effect on power output and its potential causes.

PC measurements are often used for characterisation of solar cells. However, these measurements are not usually spatially resolved, and simply serve to provide information on a cell's operating characteristics. For example, a standard procedure is to irradiate the entire area of a solar cell with an AM1.5 light source and obtain the integral photocurrent response from the entire cell.

The scanning method used in this thesis involves rastering a laser beam over the surface of the NW array solar cell. The schematic below illustrates this rastering method:

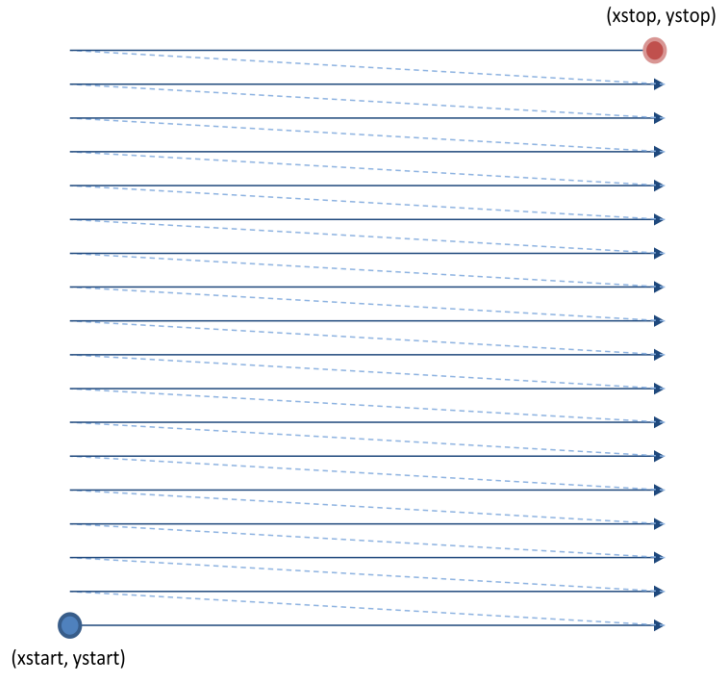

Fig. 13 - Raster scanning: dark lines (line scans) indicate where the laser moves while recording data. Dotted lines indicate where the laser moves to the next line in preparation for a line scan

The goal of this thesis is to develop a technique which provides information on the contributions of local regions of an NW array cell to the total device current. Thus, spatially-resolved PC measurements are required, and this will be achieved by rastering a focused laser; selectively irradiating small regions of the photovoltaic device under analysis, and measuring the total current contributed by the region directly under the laser beam. A sufficiently small spot size will be required to maximize spatial resolution.

4.7 Literature Review

There is very little published literature specifically related to the topic of scanning photocurrent mapping of NW array solar cells.

The earliest example of scanning photocurrent microscopy (SPCM)[22] on a microwire PV array[23] is found in *Si microwire-array solar cells* (Putnam, M. et al., 2010) [26]. The paper confirmed negligible photovoltaic response from the growth substrate between microwires by comparing three cells with different light-trapping architectures, and obtaining spatially-resolved current maps for each of them, at a sufficient resolution to determine the PC from individual wires. SPCM also revealed suspected processing defects as indicated in Fig. 14 by black arrows believed to be NWs poorly contacted by the ITO. The increased PC from cells (a) through (c) occurs due to the introduction of schemes for light trapping, light-scattering particles between the wires, surface passivation, back-surface reflector and anti-reflection coating, most notably resulting in increased PC collection from between the wires.

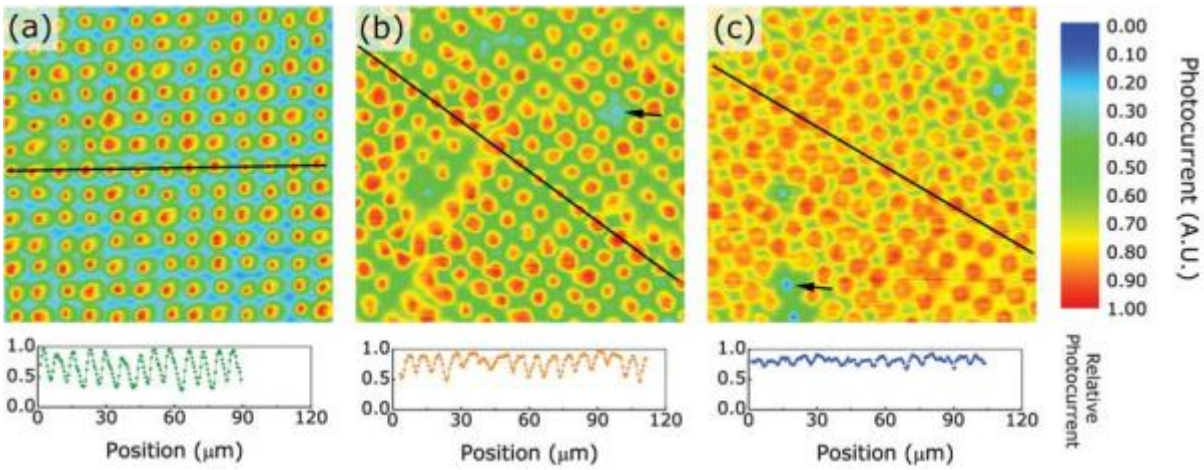

Fig. 14 - High-resolution SPCM of Si microwire array cells [26]

The SPCM was performed with a laser beam of λ=650nm and a beam waist of 1μm. The small spot size is a consideration that allows for a relatively high spatial resolution for their SPCM. However, from Fig. 14, one can calculate a relatively large 7.5μm pitch for the microwire array, which is 15 times greater than the pitch on my sample. This suggests that the ability to resolve current contributions from individual NWs may be significantly harder to achieve for this experiment.

Perhaps the highest-resolution PC mapping of a NW PV array has been demonstrated in *Patterned Radial GaAs Nanopillar Solar Cells* (Mariani, G. et al., 2011) [16]. The paper confirmed the independent functioning of each NW in the array by highly spatially-resolved SPCM, and puts non-zero current between the NWs down to the spreading of the laser spot over NW structures at such high spatial densities. The NWs in their sample are of 260nm radius, with a 600nm pitch. The SPCM was performed under zero-bias with a laser of λ=544nm, with a spot size of 400nm determined by

[22] Laser-based spatially-resolved photocurrent technique equivalent to that developed in this thesis
[23] Akin to a NW PV array, but with wires of larger thickness and pitch

full-width at $1/e^2$. The translation stage has a 50nm/step resolution. The report also highlighted the result that the technique is able to resolve features smaller than the spot size, due to the concentration of intensity at the centre of the spot, according to a Gaussian beam profile, as discussed in [31].

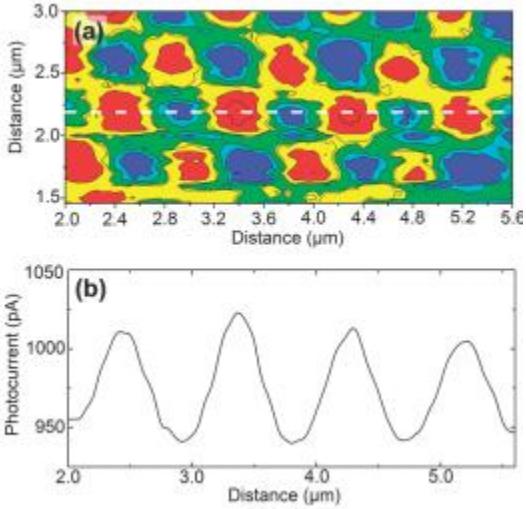

Fig. 15 - High-resolution SPCM of NW array [16]

While SPCM in the previous two cases has focused on resolving current contribution from individual wires, *Sulfur passivation and contact methods for GaAs nanowire solar cells* (Tajik, N. et al., 2011) [32] utilizes lower-resolution PC scans over larger spatial scales to determine the effect of passivation and the cell contacting regime on PC output. A laser (λ=632.8nm) with spot size 5µm was used to compare a cell that extracts current via contact fingers and one with an ITO contact layer, showing that ITO may not be the best contacting scheme due to absorption losses in the ITO layer. The paper proves that the SPCM technique can resolve features in the current signal and that those results can be meaningfully interpreted by correlating the signal with visually observable features e.g. contact fingers.

The above three papers constitute the major literature on the topic of SPCM applied to NW array solar cells, and focus mainly on high-resolution scans to resolve individual wires. Other NW-related literature surrounding the topic includes a multitude of extremely high-resolution SPCM and other scans (NSOM, AFM, STM) on two or three-terminal electronic devices of the nanoscale (single NWs) [31] [33] to determine the characteristics of individual NW p-n junction based devices. However, this kind of SPCM is removed from the topic of interest, as current research has moved beyond the stage of generating current from single NWs. Rather; techniques are now required to determine factors affecting the output of devices based on large NW arrays.

Perhaps the other most relevant category of published research relates to laser-based SPCM or other PC scanning techniques applied to large-area solar cells that are not based on NW technologies, e.g. organic (dye/polymer) cells and one notable example based on scanning a damaged crystalline concentrator cell. These studies can inform usage of scanning PC techniques when applied to NW arrays.

In *Patterns of efficiency and degradation in dye sensitization solar cells measured with imaging techniques* (Macht, B. et al., 2002) [34] laser-based spatially resolved PC was used successfully to characterize spatial patterns of efficiency and degradation of organic solar cells. Of relevance is the conclusion that spatially resolved PC yields more information than integral PC measurements, that it allows one to accumulate information rapidly, and that it can be used to visualize inhomogeneities resulting from cell processing and to determine efficiency limitations.

Patterns of efficiency and degradation of composite polymer solar cells (Jeranko, T. et al., 2004) [35] shows that spatial patterns of efficiency and degradation do occur in organic solar cells. Phenomena of interest identified on PC maps were further investigated by comparison with reflected/scattered light imaging and DEKTAK profile measurements in order to determine causes of the phenomena by ruling out morphological effects. The study indicates that spatially resolved PC maps are highly applicable to organic solar cells due to their high degree of spatial heterogeneity. It also indicates that PC maps can be used to relate efficiency patterns and their causes, concluding that higher efficiency can be reached with greater control over the contact deposition stage in the device processing. Regarding the technique, the authors agree with [34] that spatially resolved PC is more informative than integral PC measurements, and allows faster identification of defects than other techniques.

Direct Photocurrent Mapping of Organic Solar Cells Using a Near-Field Scanning Optical Microscope (McNeill, C. et al., 2004) [36] presents NSPM - a novel adapted version of NSOM to generate topographic maps with PC scans. This study indicates the benefit of correlating PC maps with other spatially-resolved maps allowing the inference of results based on the relationship between the two.

Spatially Resolved Spectroscopic Mapping of Photocurrent and Photoluminescence in Polymer Blend Photovoltaic Devices (Brenner, T. & McNeill, C., 2011) [37] concludes that there is a link between local cell composition and PC through images taken on a sub-micron region by simultaneous photoluminescence(PL) and PC mapping. The experiment performs scans over different wavelengths (spectroscopy) which provides more information and finds that for the polymer device, higher current is generated from longer wavelengths. A finding relevant to this thesis is that electrodes with different transmission coefficients affect the generated photocurrent.

Spatially resolved photocurrent mapping of operating organic photovoltaic devices using atomic force photovoltaic microscopy (Leever, B. et al., 2008) [38] develops an adapted AFM technique called Atomic Force Photovoltaic Microscopy (AFPM) to characterize an array of fully operational organic PV devices. AFM is another potential candidate for a PC mapping technique which could be applied to NW array solar cells.

Photocurrent Mapping in High-Efficiency Radial p-n Junction Silicon Nanowire Solar Cells Using Atomic Force Microscopy (Hwang, J. et al., 2011) [39] scanned the PC over a small area of a disordered Si NW forest with AFM to confirm the existence of radial p-n junctions in the NWs. The AFM technique is limited to a small scan domain.

Characterisation of solar cells by photocurrent spectroscopy and current-voltage characteristics with high spatial resolution (Schwalm, M. et al, 2010) [40] is a highly relevant study on spatially-resolved PC mapping over large areas (5mm x 5mm), evaluating the SPRS (Spatially Resolved Photocurrent Spectroscopy) technique in general. Note the distinction between Laser Beam Induced Current (LBIC) measurements which involve PC mapping without an applied voltage, and the SRPS technique which involves operation under reverse bias.

The technique is laser-based and scans a (GaIn)(NAs) concentrator cell. A laser (λ=980nm) irradiates the sample in reverse bias, with the beam focused on a 50µm pinhole, then imaged to a 30µm spot. The PC is acquired by measuring the voltage drop on a series resistor with a lock-in amplifier to remove current noise from irradiance originating from sources beyond the laser. Rastering is performed by a translation stage with accuracy of 100nm, and the resolution of the technique is found to be limited by the spot size.

The spatial resolution is termed 'high', but compared to the resolution required to resolve individual NWs, it is rather low. This helps to define the scope of the technique which will be developed in this thesis. In fact, it is the low resolution of the experiment in the paper that makes it particularly relevant for informing the development of a similar technique in this thesis.

The paper finds that local areas with defects, high impurity concentrations, and structural imperfections in the contacts can be identified by SRPS. It also identifies a number of useful measurements that can be made based on an SRPS technique. By controlling the bias in conjunction with mapping the reflectance, an EQE and IQE map of the cell can be produced. The paper also notes the importance of visually observable landmarks for orientation during scanning. Moreover, the paper indicates the importance of having a reference sample and a damaged sample for comparison in order to evaluate the technique. For the purposes of this thesis, the comparison may be made between damaged and undamaged localized regions of an NW array.

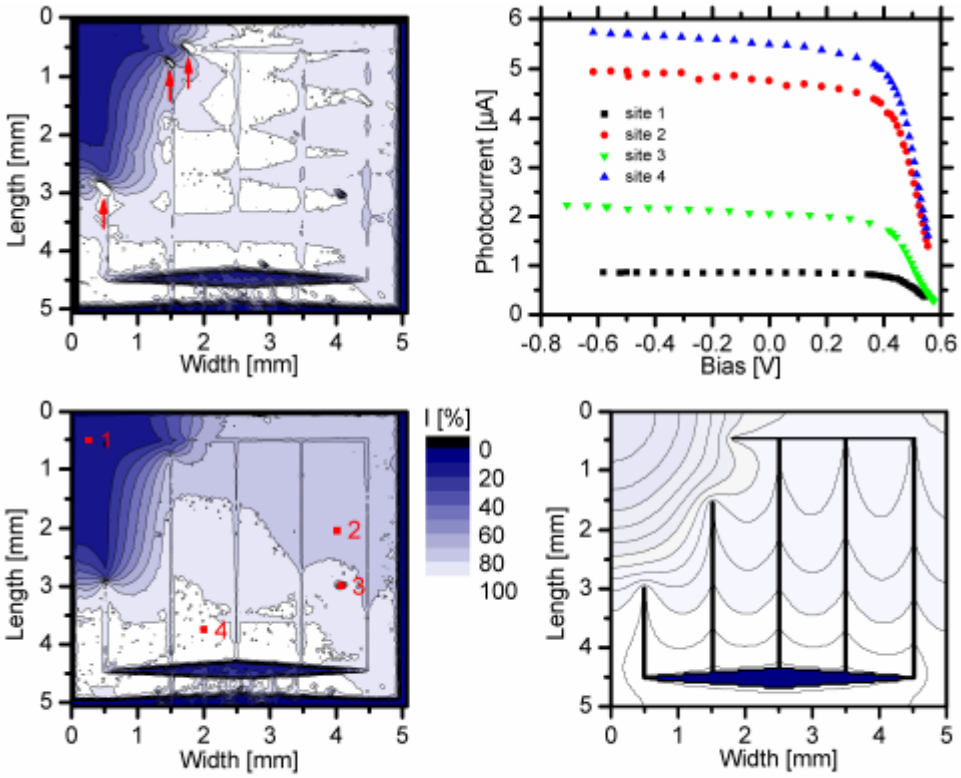

Fig. 5. Normalized SRPS maps of the damaged solar cell measured at reverse biases of 2.5 V (top left) and 0.5 V (bottom left), the corresponding simulated SRPS map at 0.5 V (bottom right) and SRIVs at different sites (top right). All maps are plotted with the same color scale.

Fig. 16 - Effects of reverse-bias on SRPS [40][24]

Of particular interest is that the paper describes the benefits of reverse biasing the sample:

1. higher signal to noise ratio
2. reduced lateral diffusion of photo-excited carriers
3. makes accessible the measurement of local characteristic parameters of the p-n junction including the short circuit current, saturation current, ideality factor, and the optically induced shunt resistance.

[24] SRIV is 'Spatially Resolved IV-Curve'

The first two effects allow for increased effective resolution, and the first for a higher scan speed. The ability to determine the effects of optically-induced shunt paths is given by performing scans and varying the bias voltage as a parameter.

The paper also discusses the importance of managing both bias and beam intensity when making particular kinds of measurements, as they affect the homogeneity of PC readings by various effects.

The literature review has identified that there has not been much work performed on spatially-resolved PC mapping over an array of NWs. This could perhaps be put down to the limited number of research groups currently capable of fully realizing NW array PV devices [15] [27].

While PC measurements have been taken on individual NWs to determine their electrical characteristics, this is largely irrelevant to the current thesis whose purpose is to enable the spatially-resolved characterization of NW array solar cells. With regard to this; various spatially resolved PC techniques applied to large-area PV devices have been described in the literature, however there is nothing corresponding to the specific application for NW array solar cells. Existing methods are not perfectly suited to this application. Thus, there is an important need for research and development of a technique for this purpose.

4.8 Thesis Statement and Scope

To develop a scanning photocurrent technique capable of spatially resolving photocurrent characteristics of NW array PV devices with speed and accuracy, and on a range of resolutions and corresponding length scales. The technique should provide information on large-scale characteristics (e.g. ITO sheet resistivity, processing of contacts), and small-scale characteristics (e.g. resolving the current from individual NWs, processing defects, local contact quality, electrical properties of individual NWs). The ultimate goal is that the technique provides information on factors affecting cell efficiency (processing defects or otherwise) in order to increase understanding and enable improvement of device performance for NW PV arrays.

4.9 Thesis Outline

The following sections of the thesis will address firstly the experimental work which has gone into developing and realizing the required photocurrent scanning technique, enabling high resolution scans of a 1mm x 1mm sample NW array solar cell. The process will be outlined with an emphasis on solutions to issues faced, serving to guide successful replication of the technique.

Major results will be presented and discussed, along with an evaluation of their significance. Moreover, the most significant issues surrounding the generation of meaningful results via the photocurrent scanning technique will be discussed.

Finally a conclusion will be presented, along with suggestions on future improvements and applications for the scanning photocurrent technique applied to NW array solar cells.

5 Experimental Work

5.1 Photocurrent Mapping Final Apparatus

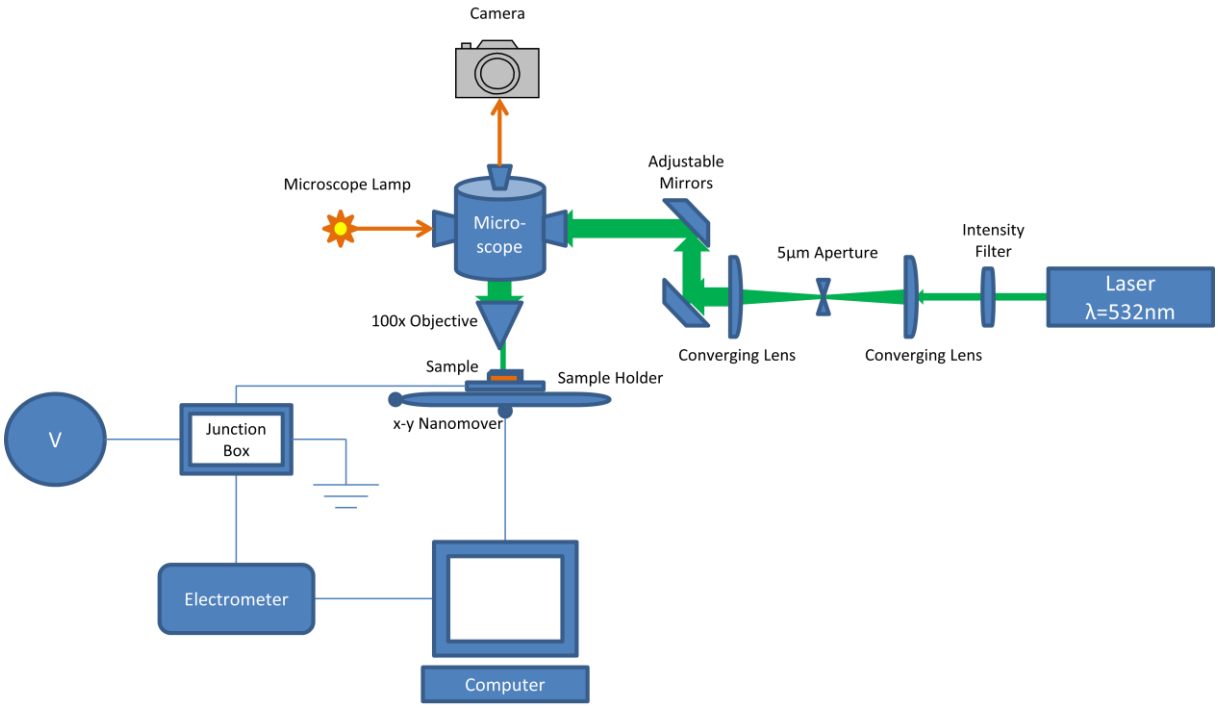

Fig. 17 - Final setup for the SPCM Apparatus

Key Components

- Laser (λ = 532nm - green), (Power = 40mW)
- Intensity Filter
- Laser spot-cleaning, focusing & alignment optics (5µm aperture on x-y-z stage), (2 biaxial adjustable mirrors)
- Optical microscope with lamp and beam pass-through – Objectives: 100x, NA = 0.8; 5x, NA=0.15
- Sample Holder
- Translation stage & x-y nanomover[25] – (resolution = 10nm/step, bidirectional repeatability = 100nm, accuracy = +/- 1 µm, velocity min/max = 5µm/s, 2.5mm/s)
- Junction Box
- Keithley 6514 System Electrometer – (sample rate = 25Hz[26])
- Computer & Software – Raster-scanning program written in LabView[27]
- Voltmeter
- Camera[28]

5.2 Development Process

The development of the SPCM with scope laid out in section 4.8 required a system to be built from scratch.

[25] Melles Griot Nanomotion II Nanomover Micropositioner
[26] Actual rate when operating in whole system – not a device specification
[27] Program written by Dan Hessman
[28] Scion Corporation Grayscale Digital Camera – CFW-1312M-IR

Design Criteria

The system must be capable of scanning for photocurrent over a range of spatial resolutions from micrometer to nanometer-scale with high speed, accuracy and precision. The photocurrent must be recorded, and stored in photocurrent maps for analysis.

5.2.1 Technique Selection

We first identified the approach which would most likely allow us to realize a device that successfully fulfilled the design criteria. Examples of apparatuses used in the literature surrounding high-resolution PC mapping provided a starting point [16] [26], and it was decided to form a device based on laser-beam irradiation of a sample mounted on a translation stage powered by a nanomover with 10nm resolution[29]. The technique has been proven to work with PC mapping of NW array solar cells [16] [26] and has demonstrated the ability to reach spatial resolutions high enough to resolve individual NWs. This approach allows for a range of resolutions by simply varying the spot size [40]. It is fast (scans typically take between five minutes and three hours depending on the number of data points chosen) and simple [34]. It does not require mechanical contact, is non-destructive, and aside from electrically contacting the device, it does not require preparation of the sample.

Other PC techniques found in the literature such as AFM were ruled out, as AFM is significantly slower, and provides a much higher spatial resolution than required [38]. In order to generate a 2-dimensional PC map, an *x-y* translation stage is used; moving the sample in a raster pattern generates the required 2D planar motion orthogonally intersecting the laser beam, and significantly reduces the optical complexity that would come with rastering the laser beam itself.

The other significant design criterion involves data capture and storage, and the scanning method. A picoammeter with a high sample rate would be required to capture the small current signal and to allow for a fast scan speed. LabView was identified as an integrated software solution which could simultaneously provide control signals to the apparatus, log data from the ammeter and store it as PC maps. Moreover, my supervisor[30] had previously written a rastering program in LabView with image-storage capability that could be adapted for use in the setup. Although lock-in amplification techniques were identified in the literature [40], it was decided to first validate the setup without adding superfluous components. Finally, a high-speed non-stop raster scanning method was chosen over a low-speed stop-start method, as this would increase the scan speed, and reduce potential mechanical vibrations induced by the stop-start motion.

5.2.2 Device Realisation

As mentioned, the apparatus had to be built from scratch.

5.2.2.1 Prototype & System Operation

The original system consisted of a green laser (λ = 532nm), intensity filter, focal optics, microscope with 10x objective, sample holder, nanomover + translation stage, junction box, Keithley485 Autoranging Picoammeter and computer with LabView rastering program.

The laser emits a beam which first passes through an adjustable intensity filter used to select the desired beam intensity. It then reflects off a two-stage biaxial mirror setup used to ensure the beam is aligned through the centre of the microscope, resulting in the tightest possible spot with minimal loss of beam intensity. Once the beam passes through the side of the microscope, it is focused by the

[29] The smallest increment (step-size) between two adjacent positions
[30] Dan Hessman

microscope optics, and passes through a 10x objective on to the sample. The spot size is determined by focusing the beam on to the sample using the microscope controls, and the irradiated portion of the sample produces a light-generated current which passes to the terminals of the sample.

The sample is bonded to a carrier chip, which is mounted on the sample holder, connected electrically to a junction box which passes the current signal to the picoammeter. In this setup, there is no biasing scheme, and the sample is electrically connected in short-circuit configuration to the picoammeter. The sample holder is itself mounted on an *x-y* translation stage, which is connected to the nanomover control box.

From this point, the physical apparatus interfaces with the computer system. The picoammeter is connected to the computer via a GPIB interface, and passes the digitized current signal data to LabView. Similarly, the computer is connected to the nanomover control box, and parameters set in LabView are forwarded to the nanomover which initiates the scan by driving the actuators connected to the *x-y* stage.

The creation of a functioning prototype required me to physically set up the apparatus with the aid of my supervisor, to learn how to use the mirrors and microscope optics to focus the laser beam to a spot, and to adapt the rastering program to correctly interface with the electronic devices.

5.2.2.2 Testing

Once a prototype had been created, it was then time to validate the setup by testing it on a well-known and understood sample. The first photocurrent scans were performed on a photodiode, whose characteristics were known, which would allow me to identify any major flaws with the setup.

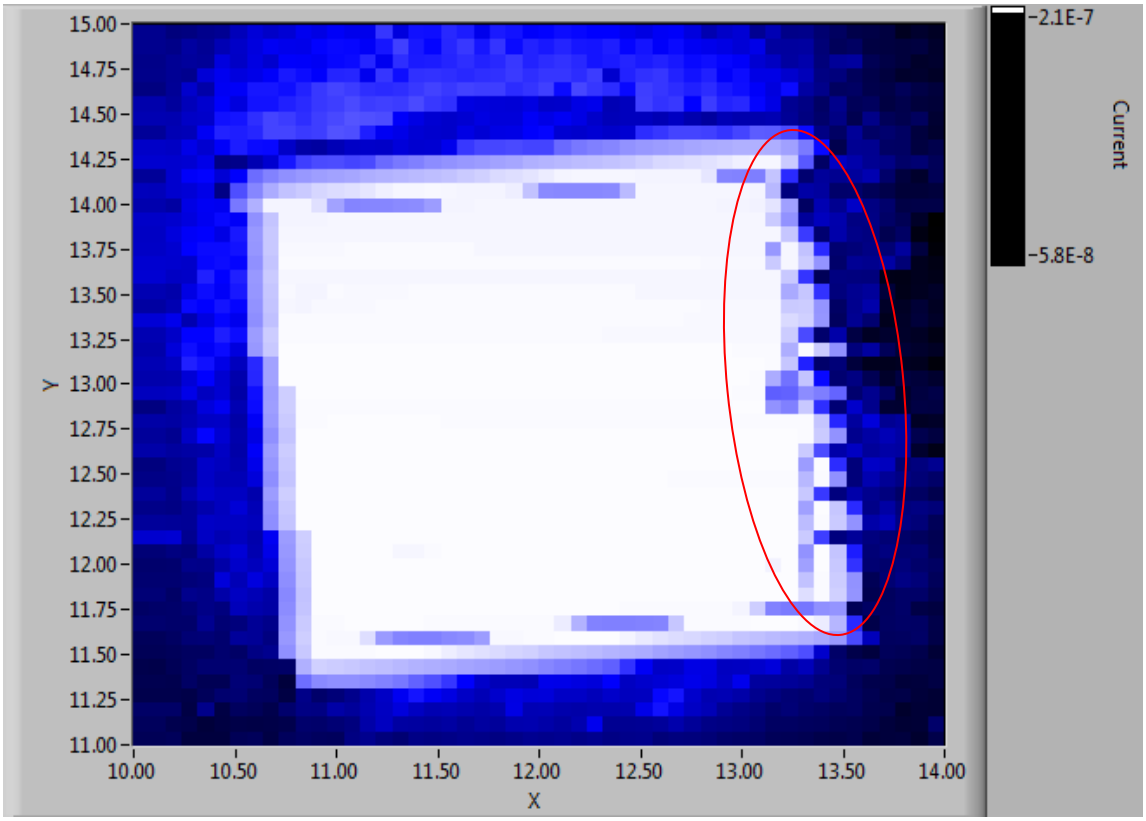

Fig. 18 - Test scan on photodiode

Fig. 18 shows the first successful PC scan of the square photodiode. This image validated the working principle, but demonstrated clear room for improvement – the resolution is quite low, and there

seem to be imaging artefacts in the current map at the right edge of the device (indicated by the red oval). NB: The colour scale has not updated to show the colour gradient which ranges from black through dark blue (low current) to white (high current). This scale is used for all subsequent PC maps.

Subsequent scans confirmed imaging artefacts and revealed bugs in the software. The right edge of the diode was scanned again in Fig. 19 (left), revealing that the blurry edge in the photocurrent map in Fig. 18 was artificial as expected. Moreover, other problems occurred when parameters were chosen to define small scan domains with high resolution, including ceased function of the motor on every second line in Fig. 19 (right), and a complete halt of the scan mid-way through in Fig. 20 (left). A high-resolution scan in Fig. 20 (right) shows poor sharpness on straight edges (indicated by arrows).

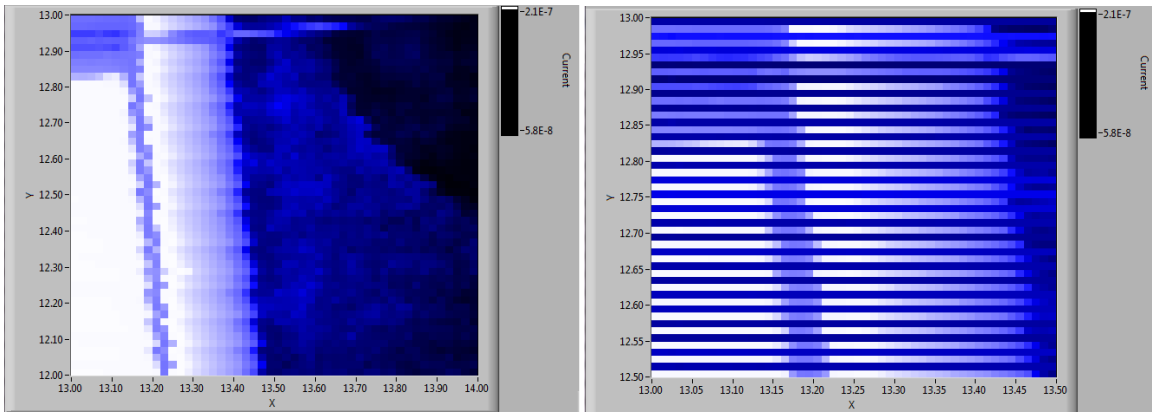

Fig. 19 - (left) Scan of the photodiode edge confirms artefacts, (right) Motor malfunctions on alternating lines

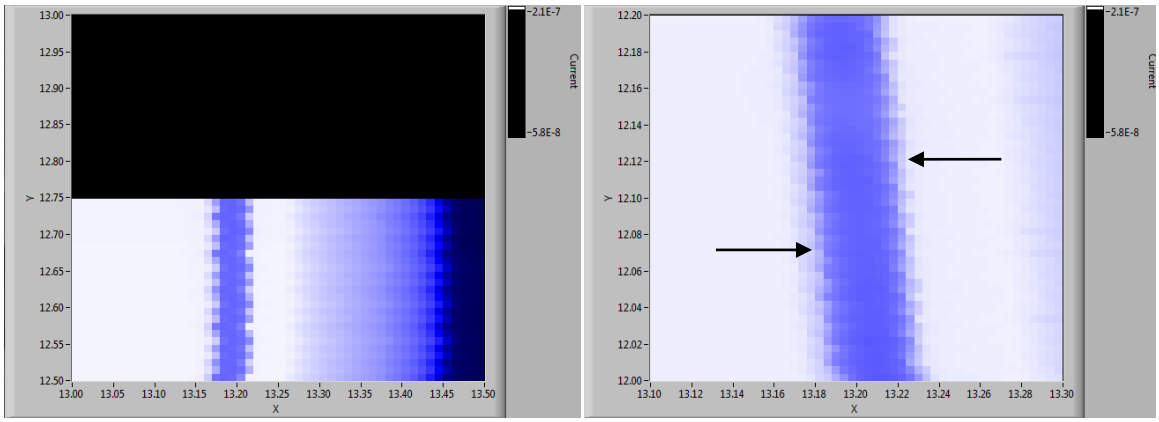

Fig. 20 - (left) Halted scan bug, (right) Successful scan with poor sharpness on straight edges

Now that the principle had been validated, a process of debugging the software followed, along with further refinements to the apparatus. Observed problems included:

- Blurry laser with a broad, non-circular spot composed of multiple maxima
- Limited allowable scan domain and resolution, beyond which bugs occurred
- Software problems including communication faults with the ammeter
- Limited scan speed – limiting factor determined to be the ammeter sample rate and communication speed

Solutions:

- Spot cleaning optics were installed, passing the laser beam through a 5µm *x-y-z* adjustable aperture to remove multiple maxima and yield a circular spot profile
- Debugging of software
- Installation of a more modern electrometer with a higher sample rate and talk speed

5.2.2.3 Revision

The testing and debugging resulted in the apparatus shown in Fig. 17, minus the camera and voltmeter.

The cleaned spot resulted in a much tighter spot diameter, increasing the possible resolution. However, the beam profile cannot be assumed Gaussian due to the multiple maxima originating from the laser itself. The 10x objective was replaced with a 100x objective for a much higher spatial resolution, and a 5x objective was added for range-finding on the sample. The 100x objective allowed for visual identification of the NW array for the first time.

The installation of the electrometer allowed for much higher sampling rates, enabling a choice between faster scans, or higher resolution scans. Moreover, this improvement resolved some of the software bugs related to communications with the ammeter and the nanomover's 5µm/s lower-limit on speed which caused scan seizure if parameters were set to scan small areas with high resolution. The minimum dwell time (the time spent scanning each pixel) was reduced by an order of magnitude from 400ms to 40ms, thus effectively making scans 10 times faster. Software had to be updated to communicate with the new electrometer.

Finally, the software debugging process had removed most of the problems which caused scans to seize up.

Some problems remained unresolved in the revised apparatus:

- Occasionally the current signal would drop to zero (or very close) mid-way through a scan
- Scans showed a high level of noise
- The sample did not sit flat on the sample holder, and caused the spot to defocus over the scan domain

Solutions:

- Although the cause for the disappearance of the current-signal was not determined, it was found that taking a voltage reading on the device would return the signal. Thus, a voltmeter was permanently installed. Moreover, the installation of the electrometer allowed for faster scans, meaning scans could more easily be completed before the time-dependent current drop-out occurred.
- The noise problem is ongoing
- The sample was propped up with a wedge of paper, providing a simple, workable solution to the problem of a tilted sample

In its final iteration, a camera was added to the setup for two main reasons:

- This decouples ocular and laser focusing, allowing the experimentalist to focus the laser spot more accurately via the camera by isolating the intensity maximum. This improves spot size and intensity.
- It allows the experimentalist to capture images to correlate with the photocurrent signal

5.3 Measurement Technique and Parameters

This section describes the process of performing a PC scan and the associated parameters used to define scans.

1. Define point of interest to scan by visual identification or deciding upon a research question.

2. Select 1D line scan or 2D raster scan.
3. Determine parameters – The corners of the scan domain: *xstart*, *xstop*, *ystart*, *ystop*; The *# of data points in x*, *# of data points in y* thus setting the pixel size (which is one of the factors that determines the limiting resolution) and scan time.
4. Set *dwell time* – the amount of time taken to scan each pixel. This determines the duration of the scan and the number of integrated current data points per pixel. The dwell time is limited by the ammeter sample rate, communication speed, pauses inserted in the programming, and the speed limit of the nanomover and its communication rate. The lowest dwell time achieved was 40ms per pixel.
5. Once parameters have been set, locate the centre of the scan domain or point of interest and focus laser spot at this point via the camera on high-contrast, low-exposure mode (to isolate the intensity maximum of the spot).
6. Select beam intensity.
7. Select voltmeter by the junction box and read V_{OC} of the device to ensure current does not drop out during the scan[31], and reset the junction box to the ammeter at a high sample rate.
8. Run the scan.

The computer then logs the data for later analysis, and comments may be added to the data file.

5.4 Evolution of Scanning Technique

In parallel to the process of upgrading the physical apparatus, was an evolution in sequential photocurrent scans which came about due to improved measurement technique and the upgrades in the apparatus itself; both informed by the scans themselves. Some of the major advances are presented here to give an idea of the iterative process of improving the quality of PC scans.

Once the technique had been validated by scanning the photodiode and fixing obvious bugs as described above in section 5.2.2.2, further scanning was performed on the NW array sample.

Fig. 21 shows two consecutive scans of the same 200µm x 200µm area. The aim was to confirm that scanning the same area with the same parameters produced the same photocurrent signal. The consecutive scans confirmed this, but it is interesting to note that the first image shows high granularity and higher contrast/more sharply defined features, with higher noise, whilst the second is smoother. Both images are taken at the same resolution, but the left image may experience higher noise because the scan was taken with the lights on. NB: Different contrast settings do not allow completely accurate comparison of the images, as can be seen by comparing scale bars to the right of each image.

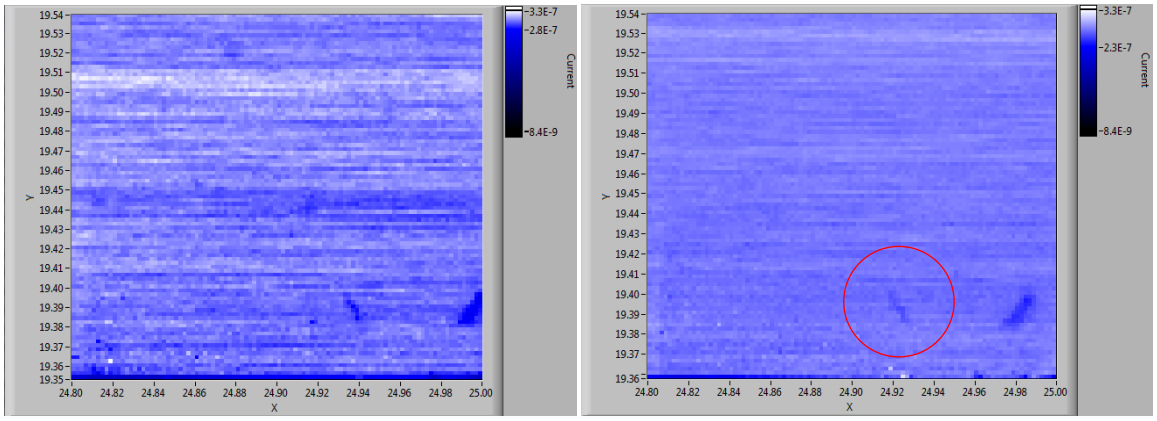

Fig. 21 - Consecutive scans of the same area - (left) with the lights on, (right) lights off.

[31] Discussed on p.29

Fig. 22 is a scan of the region in Fig. 21, slightly shifted, to determine whether the nanomover accurately shifts position, and whether the expected PC image is produced. The feature circled in both figures was identified via the ocular as the same broken NW lying across the surface of the device, and was an encouraging result. Note, however, that Fig. 22 resolved more features not visible in Fig. 21. The cause could be due to a reduction in intensity of the laser for the second scan reducing the saturation level of the current. More likely is that the spot was better focused for the features visible in the second scan. Note, also that the current signal drops out two thirds of the way through the scan.

In addition, one can see that the left side of the image contains an artefact (indicated by the box) possibly caused by the same packet of data being held in the LabView data writing interface and then stored in the PC map for a few consecutive pixels each time a new line is scanned. Recall the schematic in Fig. 13 which describes that the raster scan begins in the bottom left of the image, scanning horizontally to the right, line by line, gradually filling up horizontal lines until it is completed at the top-right corner of the image. Finally, it is worthwhile noting that the granularity and sharpness of the PC map seems to decay in the y axis, and could indicate defocusing of the spot from the bottom to the top of the scan due to e.g. a tilted sample[32].

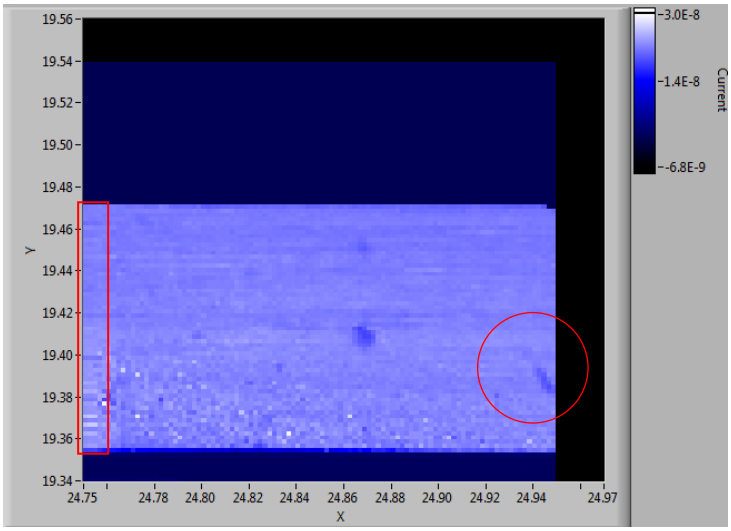

Fig. 22 - Scan of the same area as in Fig. 21, shifted slightly, shows the artefact (in the box) and the current drop-out

Fig. 23 shows the instant where a solution to the current-drop out problem was confirmed. One can see that the scan is better able to sharply resolve features such as high-current spots (white dots) and dark spots which indicate features on the device surface. However, comments made during the scan indicate that some clearly observable features e.g. broken NWs laying across the surface at the coordinates marked by the red circle in Fig. 23 do not appear as expected dark features in the PC signal.

The scan was run with the lights off, and with an even lower power setting than the scan in Fig. 22 to determine the effect of saturation on the sharpness of the resulting PC map. The conclusion was that a balance of intensity must be found to ensure high contrast – a higher intensity produces a signal with larger magnitude fluctuations between high and low PC regions, but an overly high intensity may saturate the current reading.

The dark band at the bottom of Fig. 23 is one of the metal contacts, and results in a 0A current reading as no light is absorbed beneath the contact. However, two-thirds of the way through the scan, the signal abruptly drops to the same 0A current reading where there should be no obstruction

[32] Discussed in section 6.8

on top of the active area of the device. I only entered the room near the end of the scan, and connected the pins of the voltmeter across the sample while the scan was still in progress, to see if this brought back the current signal as I suspected it would. One can see that the signal suddenly reappeared and that each time I connected the pins thereafter (indicated by orange arrows), a current reading of 0A was produced as indicated by the black dots and lines at the top of the image. The cause for the drop-outs is as-yet undetermined. Note also that the smearing artefact at the beginning of scan lines (indicated by the box) is still apparent in Fig. 23.

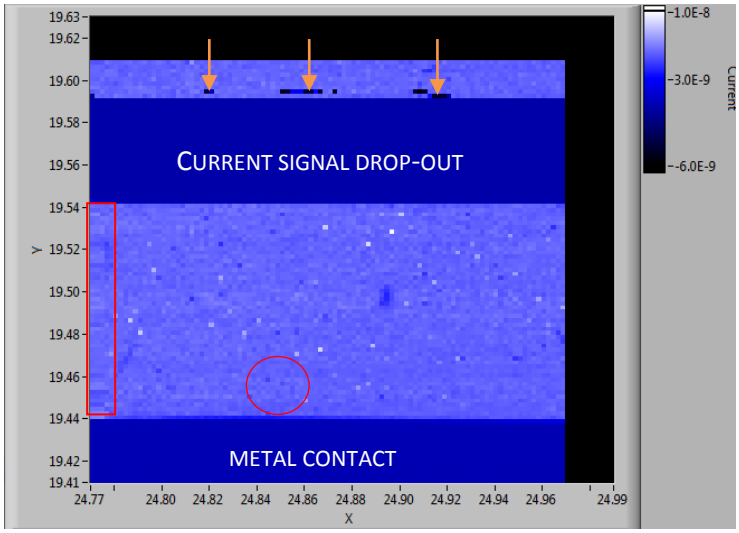

Fig. 23 - Current drop-out problem resolved - after reading V_{OC}, the current signal returns

The scan in Fig. 24 was conducted to solve a variety of questions. Firstly, the scan domain was set to pass over a portion of the same region where the current signal drop-out occurred in Fig. 23 in order to establish whether it was a non-physical effect. This was confirmed by the existence of a current signal in that region. The scan was shifted to confirm whether the artefact on the left hand side of the previous scans was non-physical. This was confirmed by its continued appearance in the PC signal (indicated by the box in Fig. 24), proving no correlation to the device region under analysis. Moreover, for this scan, the sample was adjusted and propped up so that there was no significant deviation in tilt angle over the scan domain, and thus no defocusing of the spot over the PC map. This is evidenced by a uniform sharpness over the entire scan domain. Nevertheless, the current-drop out issue persists, and one can see that it is a time-dependent phenomenon, always occurring after a similar duration into the previous few scans (which all have the same length and time parameters).

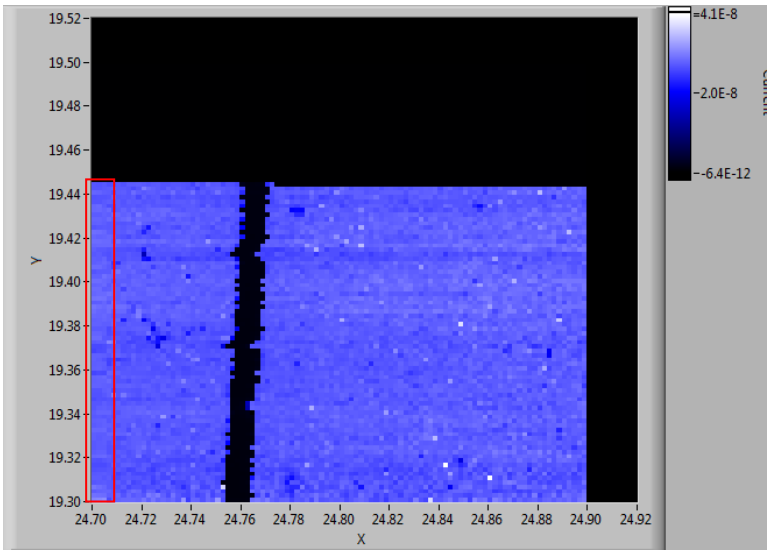

Fig. 24 - Low power scan over a gold finger (diagonal black band) confirms the persistence of artefacts and drop-outs

A wait time was added to the program, in order to allow the ammeter time to communicate at the end of each line, in the hopes that this would allow it to clear garbage data from memory before sending new data to the computer at the beginning of the next line. This had no effect on the artefact at the left hand side of all five previous scans.

A significant upgrade to the system was achieved when the electrometer was installed and tested. Fig. 25 shows the first scan of the whole device, made possible by the 10x increase in sample rate. Note the current signal did not drop out before the end of the scan. Some new artefacts appeared – most notably, small diagonal current fluctuation patterns running from the bottom left to top right corner of Fig. 25. One can also observe horizontal bands of high and low current.

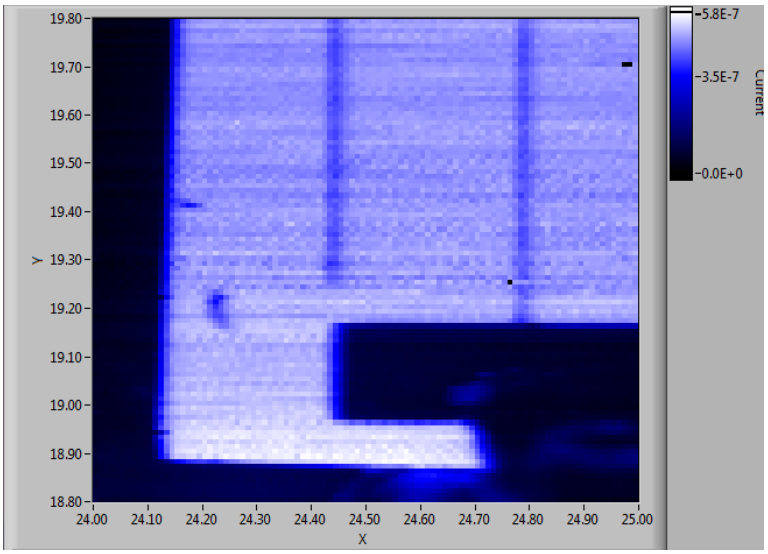

Fig. 25 - First scan of the whole device scan with the electrometer

Fig. 26 investigated the performance of the electrometer at smaller length scales (50µm x50µm) and higher spatial resolution than previously attempted. This demonstrated that the electrometer allowed for scan areas small enough that features (such as the white dots indicating high current) of ~800nm scale could be resolved, but with a high level of noise, including aforementioned horizontal streaks and bands. Moreover, the electrometer does not display the artefact at the beginning of each new line, indicating the artefact originated in the ammeter and its communication interface.

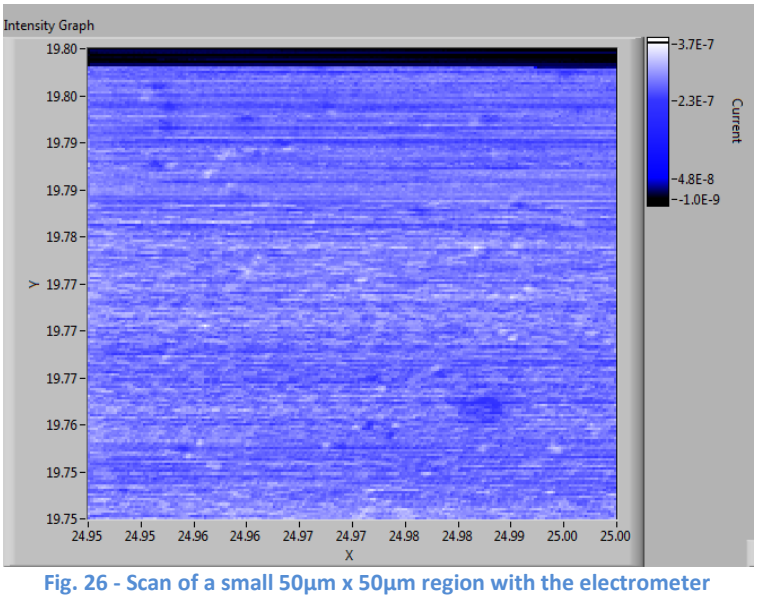

Fig. 26 - Scan of a small 50µm x 50µm region with the electrometer

Continued improvements to the scanning technique included realigning the laser to produce an optimally focused spot, minimizing the tilt angle of the sample to minimize resolution loss, and a more standardized approach to conducting scans, as laid out in section 5.3. This eventually allowed for high resolution scans over large areas (1mm x 1mm in Fig. 27) and small areas (100µm x 100µm in Fig. 28 with pixel size 200nm by 200nm).

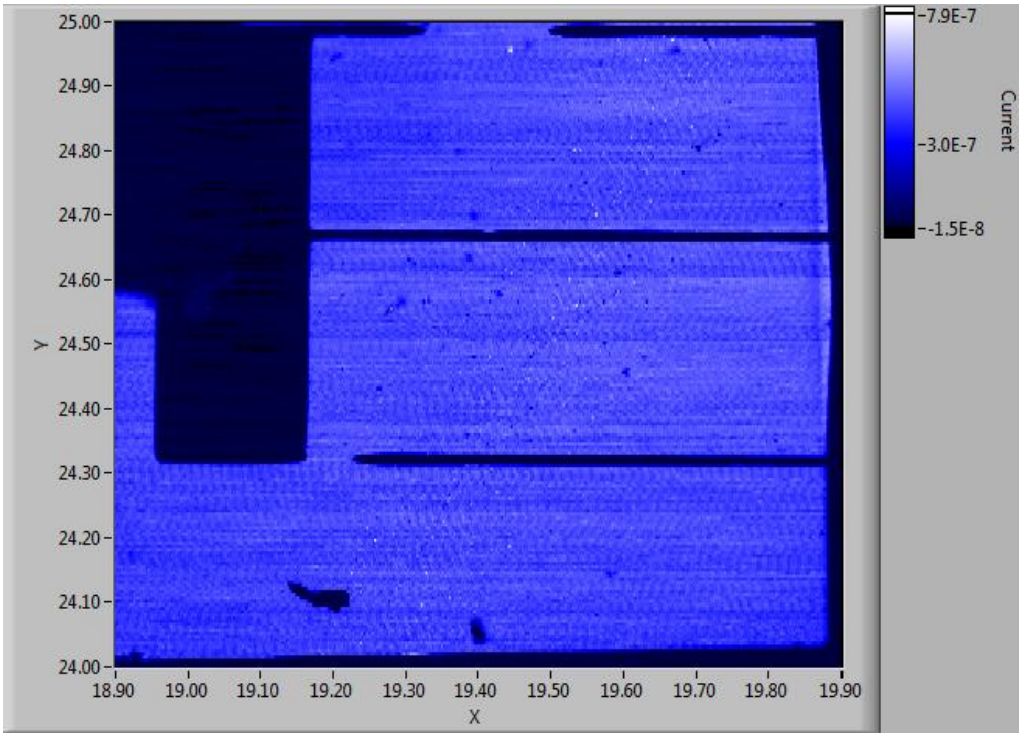

Fig. 27 - Fast scan of the whole device (1mm x 1mm) with pixels of dimension x=2.5µm, y=5µm

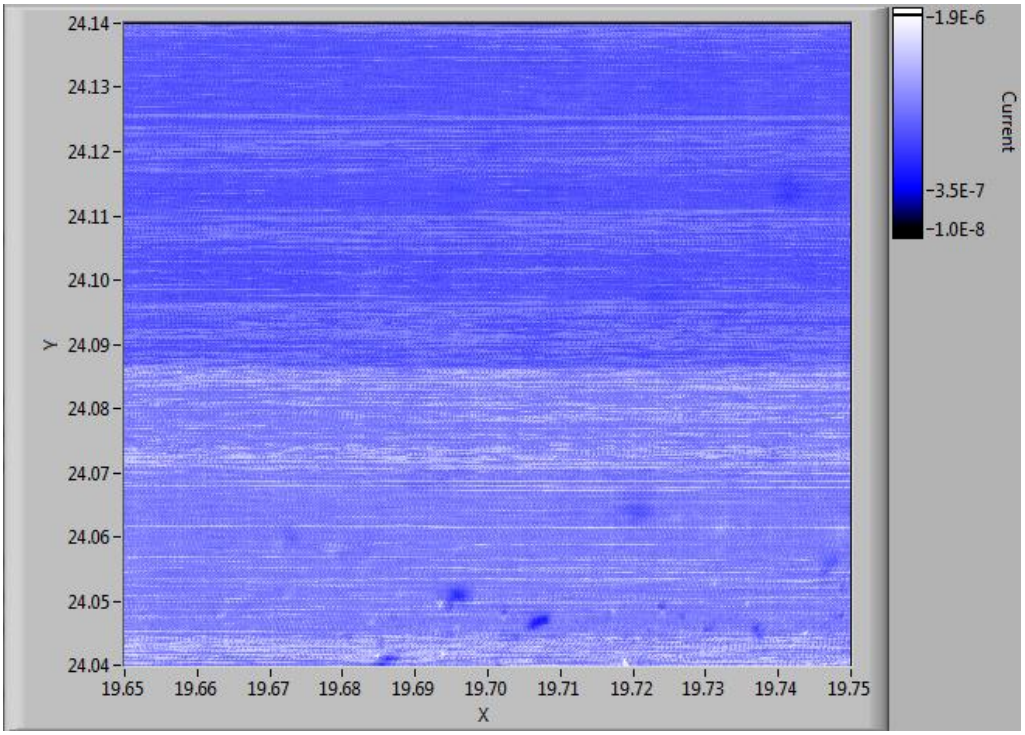

Fig. 28 - High resolution scan (100µm x 100µm) with 200nm x 200nm pixels

This concludes an outline of the development process behind the PC scanning technique. Further scans with meaningful results will be discussed below in section 6.

5.5 Bonding

Bonding describes the process of mounting and electrically contacting the sample to the carrier. This procedure was required during the course of the experiment on two separate occasions – once due to a handling-induced breakage of the sample's interconnecting wire, and once due to a failure of the sample to produce a voltage or photocurrent, indicating a short circuit or faulty contact. This section describes some of the problems encountered, focusing on solutions to the difficult process of bonding to NW array solar cells.

The 'device' consists of multiple isolated 1mm x 1mm NW array solar cells in a grid pattern on an InP substrate. The 'carrier' is a mount on to which the back contact of the device is glued with silver paste. To complete electrical contacting of the sample, a thin bonding wire must be attached between the back contact and one of the pins on the carrier, and another bonding wire must be attached between a different pin, and the metal contact pad on the front surface of the 1mm x 1mm NW array solar cell to be analysed via the PC scanning technique. Fig. 29 shows the 1mm x 1mm cell below:

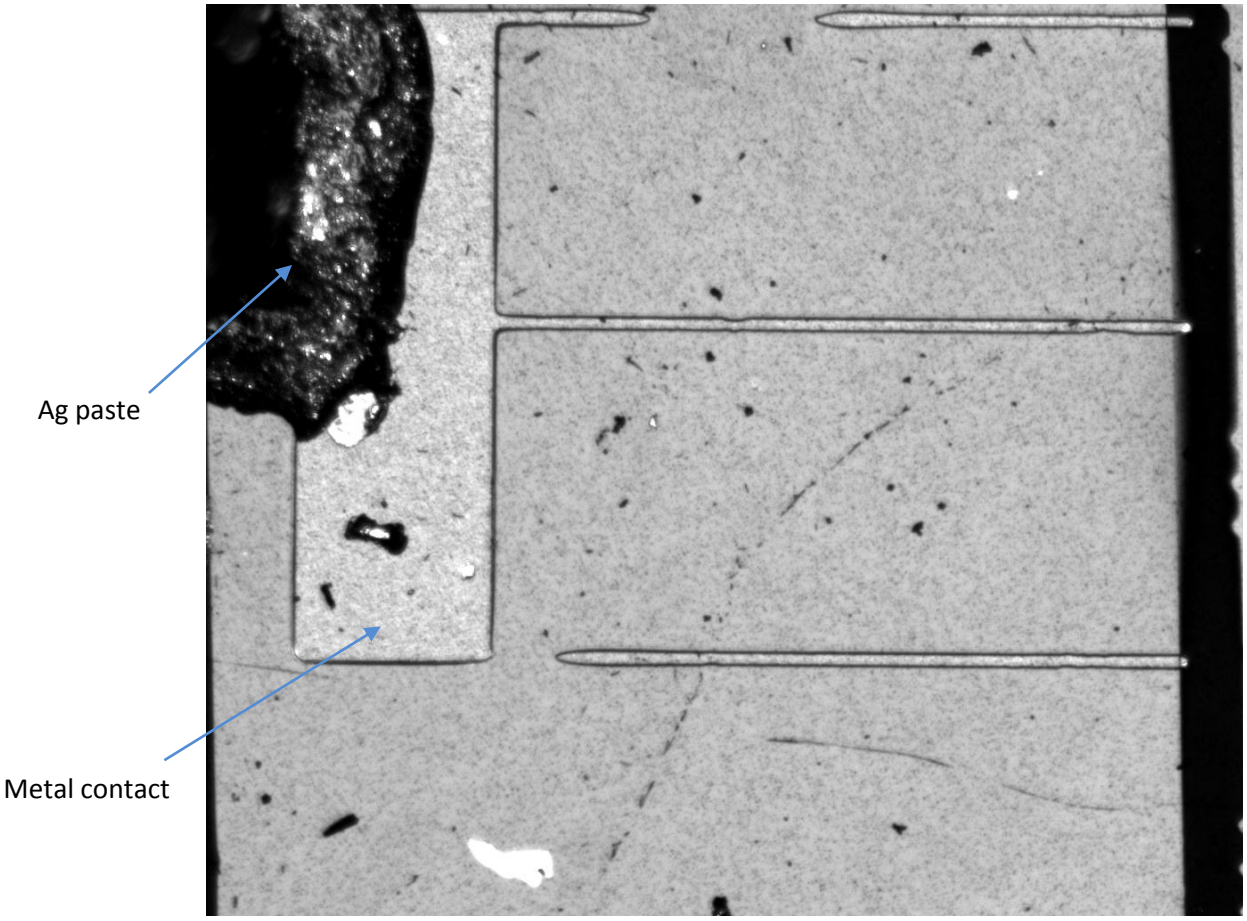

Fig. 29 - Camera image of the whole 1mm x 1mm NW array solar cell device

The process of connecting the back contact and the pins is rather trivial – there exist fully functional bonding devices with microscope optics and micrometer controls with which one can easily and systematically achieve bonding with most ordinary devices.

However, a difficulty arises with NW solar cells in that the bonding device is not suited to the metal contact pads used on the sample, and hence bonding to this final contact could not be achieved via this approach.

The metal contact pad can be seen in Fig. 29, wherein it is the partly obscured large rectangular element on the left side of the image. Its dimensions are 0.2mm x 0.7mm, and the obstruction seen in the figure is actually the dried silver (Ag) paste ultimately used to successfully glue the bonding wire to the contact.

Difficulties

NW array devices are highly susceptible to mechanical breakage. Due to the vertical architecture of a NW array, any slight mechanical pressure from above can cause breakage of NWs and lead to shunts and even a catastrophic short-circuit of the NW device. Moreover, due to the proximity of the contact pad to the active NW array and the small length scales involved, great care is needed to ensure no mechanical force is imparted to the surface of the device.

Thus, short of developing a scheme to situate the bond pads further from the NW arrays, and to increase the area of the pads, a soft-bonding technique is required whereby mechanical force is minimized.

Approach

The method used involves holding the wire to the contact, and wetting the two surfaces with liquid silver (Ag) paste, keeping them in proximity until the solvent dries, gluing the wire to the pad.

Initial attempts to bond via this method involved using a hand-held toothpick to deliver the Ag paste, with the bonding wire held in place by hand-held tweezers under an optical microscope. The approach was at first successful in achieving bonding, but there was no control over the amount of Ag delivered – the droplet spread out, completely covering some of the adjacent NW array cells on the device. Moreover, the procedure is still very difficult, and even the most steady hand might run the risk of damaging the device.

A bonding assistance device was realized, which consists of an *x*-*y*-*z* stage to which a sample holder is attached, allowing precise control of the sample by micrometer screws. An arm which is stationary with respect to the user extends over the device, and holds the bonding wire in place with a small screw chuck. The contact pad on the device can be positioned in very close proximity to the wire tip, and subsequently, one can apply the bead of Ag paste, only having to coordinate one moving part, simply waiting for the paste to dry before using the device again to bond the other end of the wire to the contact pad for the pin on the chip carrier.

Considerations

Despite the aid of the bonding assistant, many factors still act to make the bonding process difficult. Firstly, it is still very difficult to control the bead size, and multiple approaches (sharpening a toothpick into a fine-point applicator, using a thin diameter wire, creating a funnel) did not yield a reliable and repeatable solution. If one makes the bead too large, it will spread over the device during the wetting stage. If one manages to isolate a drop that is sufficiently small such that it will not spread out over the NW array device, it usually dries so quickly that it is solid before it can wet the surfaces. Even if a drop of perfect size is isolated, and applied to the contacts, it usually 1) prefers to stay with the surface of the applicator when the drop has been applied and the applicator is removed or 2) is semi-dried before wetting and does not form a good contact.

A possible simple solution to this fundamental problem is to perform the procedure under a cold fluorescent lamp so that drying time does not become a factor in the bonding.

Outcome

By trial and error, one cell was finally bonded successfully to the carrier, and this cell was used for all experiments on which the scans presented in this thesis were based. Nevertheless, the device was subject to significant handling damage, and multiple cells were destroyed in the process before bonding was achieved. Damage from the bonding process resulted in broken NWs, scratches and scattered flecks of dried silver paste littering the surface of the sample, and the damage may have reduced the overall shunt resistance of the cell, as evidenced by the low V_{OC} = 230mV which the cell outputs in comparison to its rated V_{OC} of 330mV.

Thus, the results gathered herein are based on scans of a non-ideal NW array solar cell. However, as indicated in [40], this superfluous damage in fact provides benefits for the evaluation of a spatially-resolved photocurrent scanning technique – the damage provides features which can be resolved in the photocurrent, which provide landmarks for orientation, and in comparison with uniform undamaged regions, can be used to evaluate the efficacy of the technique.

6 Results & Discussion

The results presented here primarily take the form of photocurrent maps which were selected based on whether they validate or satisfy the different aims of the thesis. There are a great many conclusions that can be made from the scans performed, so I will make my best attempt to keep the results and corresponding discussion organized and focused in scope.

In general, I will begin with the obvious results which validate the efficacy of the PC scanning technique, and then move from presenting results of large-area scans towards small-area scans at higher resolutions, honing in on the limitations of the technique which are more apparent at shorter length scales.

6.1 Efficacy of the Technique

One of the most obvious results for this thesis was the realization that the technique works. After the lengthy development process, scans were finally produced which achieved the aims of the thesis – they demonstrated the ability to spatially resolve photocurrent characteristics of a NW array solar cell. As required, the scans were clear, fast and demonstrated proof of concept. PC maps of this type have already been presented in section 5.4, in particular Fig. 27 & Fig. 28

The high-resolution scan of the whole 1mm x 1mm device in Fig. 27 is presented again here as Fig. 30, but not just to reiterate the obvious result that scanning PC mapping works. One of the stipulations in the thesis aim is that the technique specifically provides information on a large length-scale, about large-scale characteristics. In particular, Fig. 30 will be further discussed with regard to how it informs one about factors affecting cell efficiency. It is a useful result to show that a technique works, but infinitely more valuable to show that the technique can provide information on the link between features on the PC map and their effect on cell efficiency. Thus, the technique can prove its usefulness by identifying for example processing defects which impact the current output.

Moreover, Fig. 30 is not presented here in isolation. Rather, it is presented beside a camera image of the exact same area (Fig. 31) to show that the photocurrent technique can be used to provide a myriad of information on the device, particularly when analysed in conjunction with other forms of imaging – a notion which was made apparent by reviewing the literature, as discussed in section 4.7. The following two images together yield some significant results.

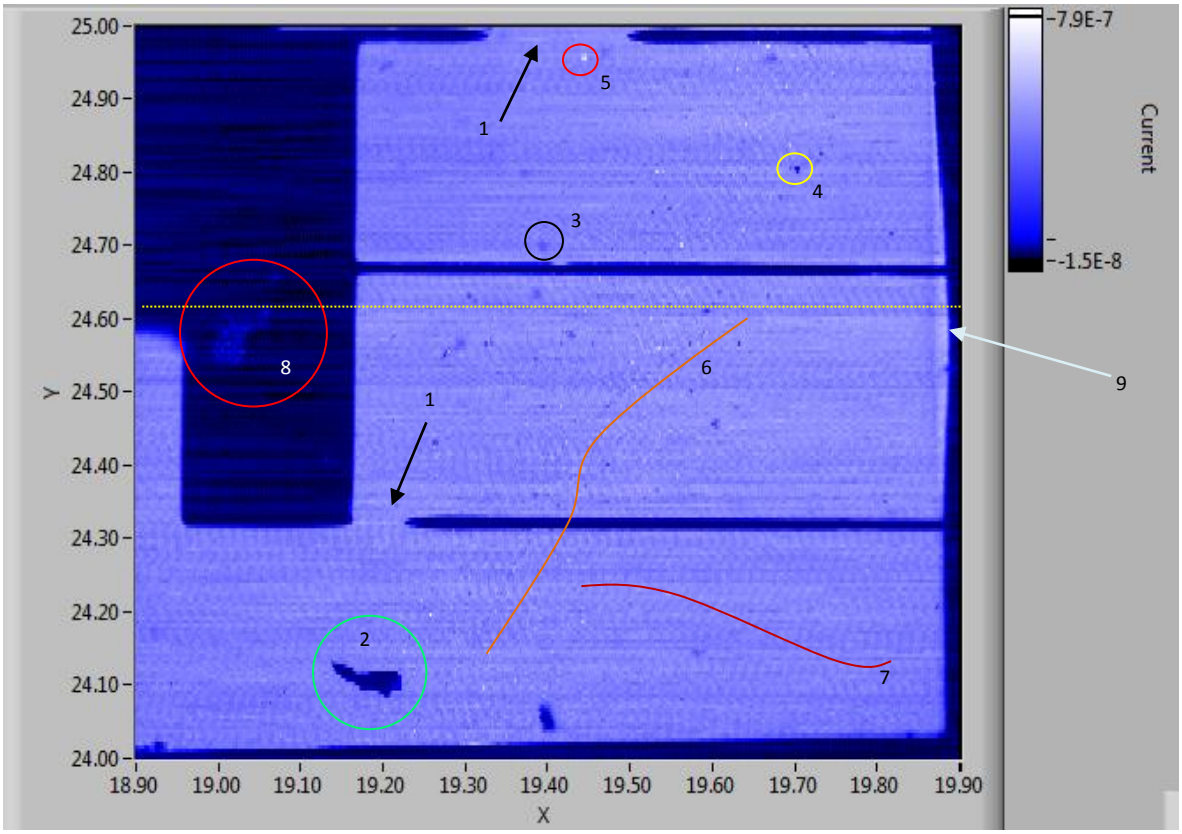

Fig. 30 - High resolution PC map of the 1mm x 1mm sample NW array solar cell

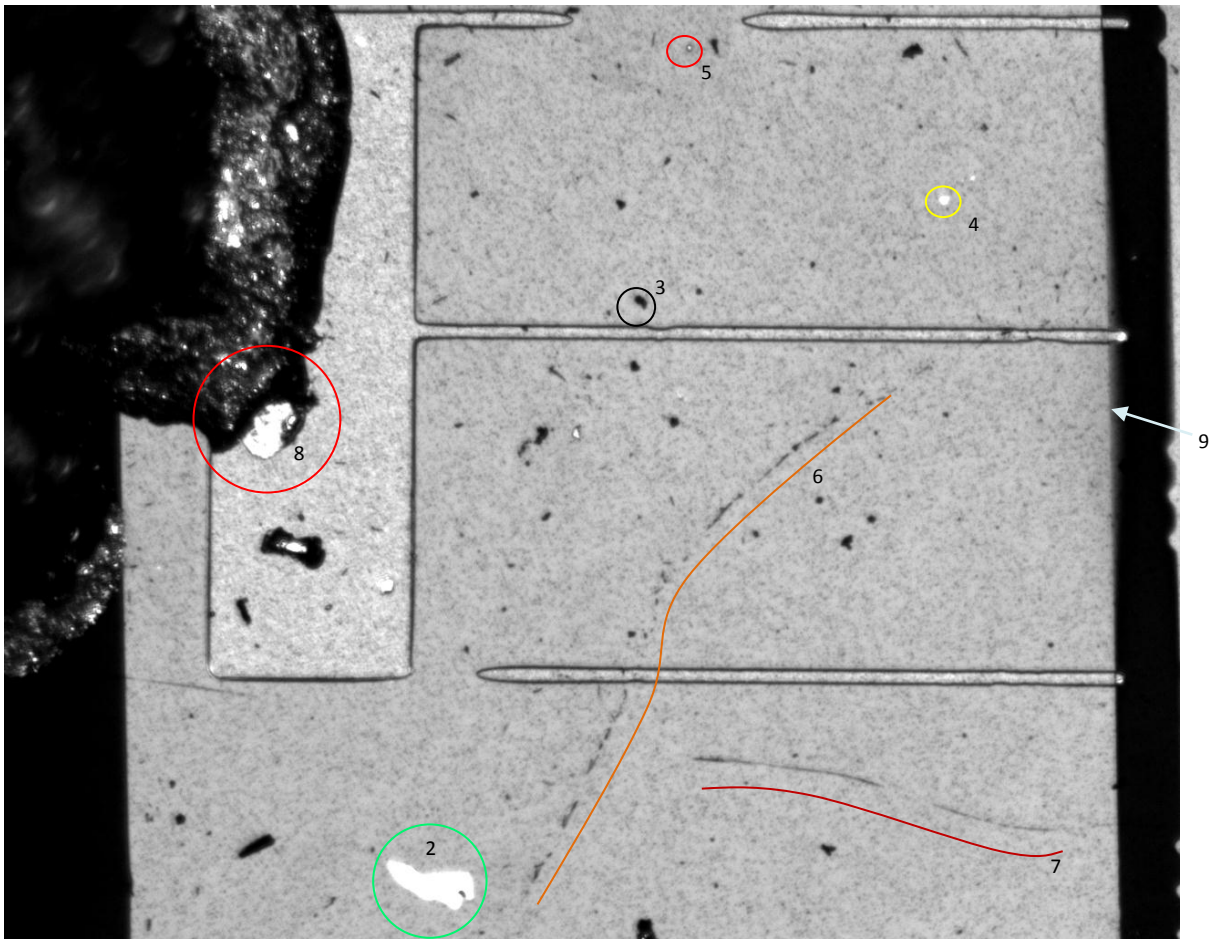

Fig. 31 - Camera image of the 1mm x 1mm sample NW array solar cell

Seeing the images side by side, a first result is the confirmation of the fidelity of the PC map – the PC map accurately represents the sample being imaged, and this both serves as a sanity check and shows that visible features can be correlated with their effect on current output.

Whereas the camera image merely shows visible features, the PC map relates them to their effect on the output of the cell. For example, it is clear that any area covered by the large opaque metal contacts generates no current.

Immediately, one can identify a large-scale processing defect on the device from both images – the lithography and metal evaporation clearly failed, and resulted in incomplete fingers, indicated by the two black arrows (1) in Fig. 30. As the PC map shows, these fingers do not noticeably contribute to any improved current output, and simply serve to cover the cell, reducing total output. However, it is hard to discern from the PC map alone whether the current contribution from local regions of the array are affected by their proximity to finished or unfinished fingers, and whether the failed fingers result in reduced short circuit current compared to the finished finger.

Another large-scale feature is clearly evident in the PC map – the dark patch indicated by the green circle (2) in both Fig. 30 & Fig. 31. It is clear from the PC map that this region generates no current. Moreover, as previously discussed, further understanding can be gained by correlating images obtained from different techniques. For instance, observation through the microscope shows that this is most likely a processing defect and not damage-related. There are no signs of broken NWs or scratches. The patch is visually determined to be a thin layer on top of the ITO[33], and is green in colour during visual observation. A third method of analysis is the camera image, which indicates that the patch is highly reflective, and this allows one to deduce that the mechanism by which it reduces output current is because it transmits very little light through to the NW array beneath it.

It is interesting to notice that not all features behave in the same manner. As discussed previously, significant damage was inflicted on the cell during the bonding process, and as such, the surface is littered with broken NWs, flecks of dried silver paste, scars and pits. These different types of damage generate different effects in the PC signal. As an example, three small circles in the top portion of each image have been used to indicate correlated features. The black circle (3) corresponds to a fleck of silver covering the cell. It shows up as a dark shadow in both the PC and camera images, most likely indicating that light hitting it is scattered away from the camera detector and also prevented from reaching the NWs beneath it. The feature in the yellow circle (4) shows up as a bright spot on the camera image but a dark spot on the PC map. It could be a feature that exhibits high specular reflection, like the feature in the green circle discussed previously. Meanwhile, the red circle (5) denotes a feature that shows up as a bright spot in both the camera image and PC map. The feature has been identified as a large processing-related pit where NWs have failed to grow. The bottom of the pit is reflective, and as discussed in section 6.4, there is some phenomenon which causes a higher photocurrent to be produced when the pit is illuminated compared to when the surrounding array of NWs is illuminated.

If one looks for the dark scratch (6) parallel to the curvy orange line on the camera image, one can just make it out in a similar position relative to the same orange line on the PC signal. The line is a scar where NWs have been ripped out, and thus it is incapable of producing current. This is not so obvious from a camera image, which shows that light is not reflected from the scratch back to the camera, so it must either be absorbed or scattered, which is inconclusive with respect to the scratch's effect on current generation. Clearly, from the PC map, the absorption is not resulting in generated current. Interestingly, a similar scar (7) indicated by the maroon line does not show up in the PC signal. This is either because the scar does not result in reduced current generation, or

[33] Topography can be inferred from the focal depth required to resolve the image

because of some other effect. It turns out this is most likely due to an effect related to the rastering method and scan direction, as discussed in section 6.2.

Another result from the scan has been indicated by the large red circle (8) in both images. From the camera image, one can see that there is a large Ag blob which is used to contact the device, and clearly covers the NW array (which would be covered by the metal contact anyway) such that one would expect no current signal to be measured when the laser scans over it. However, in the PC map, there is a region of increased current detected there. The result indicates the importance of understanding the technique, and carefully considering its complexities when performing analysis. The most likely cause is that when the beam passes over the highly reflective blob, light is scattered on to the surrounding active areas of the cell which absorb the scattered light and contribute to the current signal. This also brings to light the implications of surface topography for the technique, some of which are further discussed in section 6.8.

An interesting large-scale feature is indicated by the arrow (9) on the right side of both of the figures, pointing to a region of high current at the extreme right edge of the cell. Although nothing can be detected from the camera image, there is clearly an increase in the current signal from this zone which is above any discernible level of noise. While I cannot offer an explanation as to the cause of the increased photocurrent, it is potentially a fruitful discovery, and should be further examined to determine the cause.

A further note should be made on the noise and artefacts discernible in the PC scan. There is a clear texture pattern on the PC map in Fig. 30 that cannot be put down to any physical effect. Although the cell is based on a NW array, at this scale, peaks and troughs in the current signal from individual NWs (as in Fig. 14 & Fig. 15) should not be visible, and there are otherwise no indicators from the camera image or ocular that an oscillatory signal should be observable on the PC map.

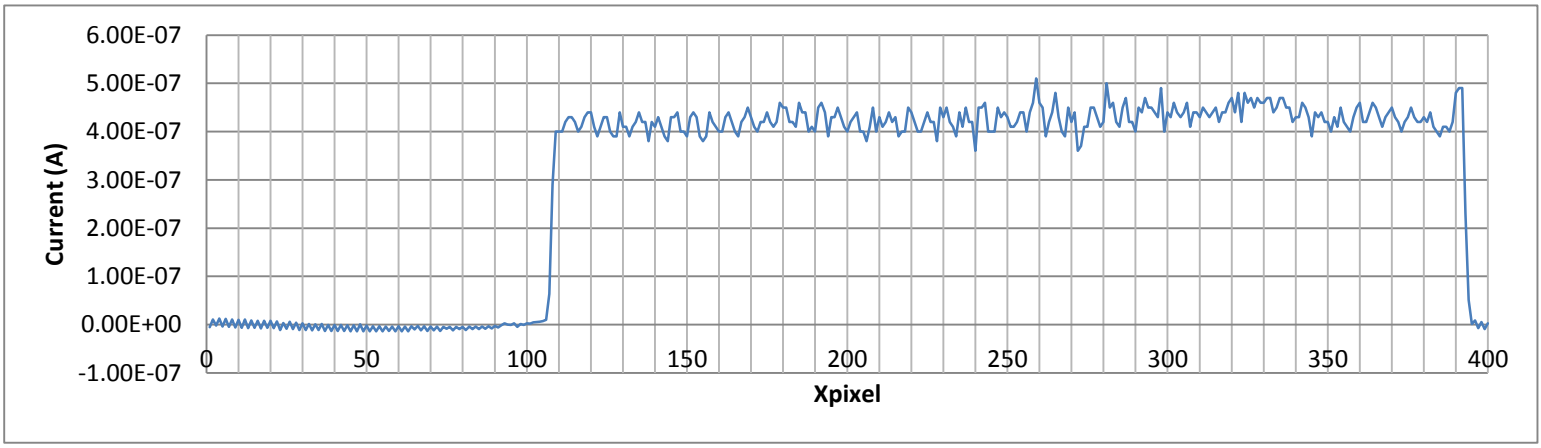

Fig. 32 - Line scan from Fig. 30 over domain x ∈ [18.90, 19.90] indicates oscillatory current fluctuation

The oscillatory signal is demonstrated in Fig. 32, which is a line scan through the section indicated by the yellow horizontal line (Y = 24.62mm) in Fig. 30. Firstly, in the region of zero current at the metal contact, there is a minor oscillation in the current signal that is most likely noise originating in the electrometer. Due to the scaling in Fig. 30, one can make this out as horizontal patterns of small blue dots, and from data analysis, the tiny oscillation alternates between a peak and a trough from each pixel to the next. This noise pattern is systematic and regular, and underlies the whole PC map, not even changing from one line to the next (if one looks closely, one can see vertical lines in the scan, indicating that the noise pattern begins at the same point in every line scan, and oscillates with unchanging periodicity). Because of its regularity and tiny amplitude, this noise pattern could potentially be subtracted from the scan data and is thus a minor issue.

On the other hand, there is a larger pattern of oscillation that is visible on the PC map in the region where the cell is producing current. As shown in Fig. 32, this oscillation occurs with longer periodicity, and significantly alters the signal from what one would expect to be a relatively spatially homogeneous current. This noise will be further analysed in section 6.5 with regard to how it affects the capacity to draw worthwhile conclusions from PC maps.

Other noise-related phenomena visible in Fig. 30 or more obviously in Fig. 28 include 'streaking' which refers to variations in current over time scales corresponding to roughly one line scan, appearing as horizontal streaks of about one line in thickness; and 'banding' which refers to a similar phenomenon over longer time scales, appearing as alternating horizontal bands of higher and lower current which significantly alter the PC signal. These effects are examined in detail in section 6.5.

Analysis of this scan (Fig. 30) in conjunction with a camera image has revealed much about the scanning photocurrent technique and its strengths and possible weaknesses. In particular, the key results are that the spatially resolved PC mapping technique works; it can map relatively large areas quickly and accurately, can resolve large-scale features which affect the current and in conjunction with other techniques can help identify the type of defect or enhancement which shows up in the PC signal. Importantly, via the PC map, links can be made between features and their effect on cell efficiency. Some limitations to the technique are hinted at – in particular, the existence of a multitude of noise patterns both regular and irregular which might obscure smaller signal fluctuations, and the artefacts that surface topography can generate in the PC map.

At this point, it might be beneficial to recall that in general, one can identify two main causes for fluctuations in the PC signal – interactions with the laser beam before absorption of photons in the p-n junctions, and then electrical properties post-absorption. On large scales with low resolution, the technique seems to be able to resolve more information related to the former phenomenon.

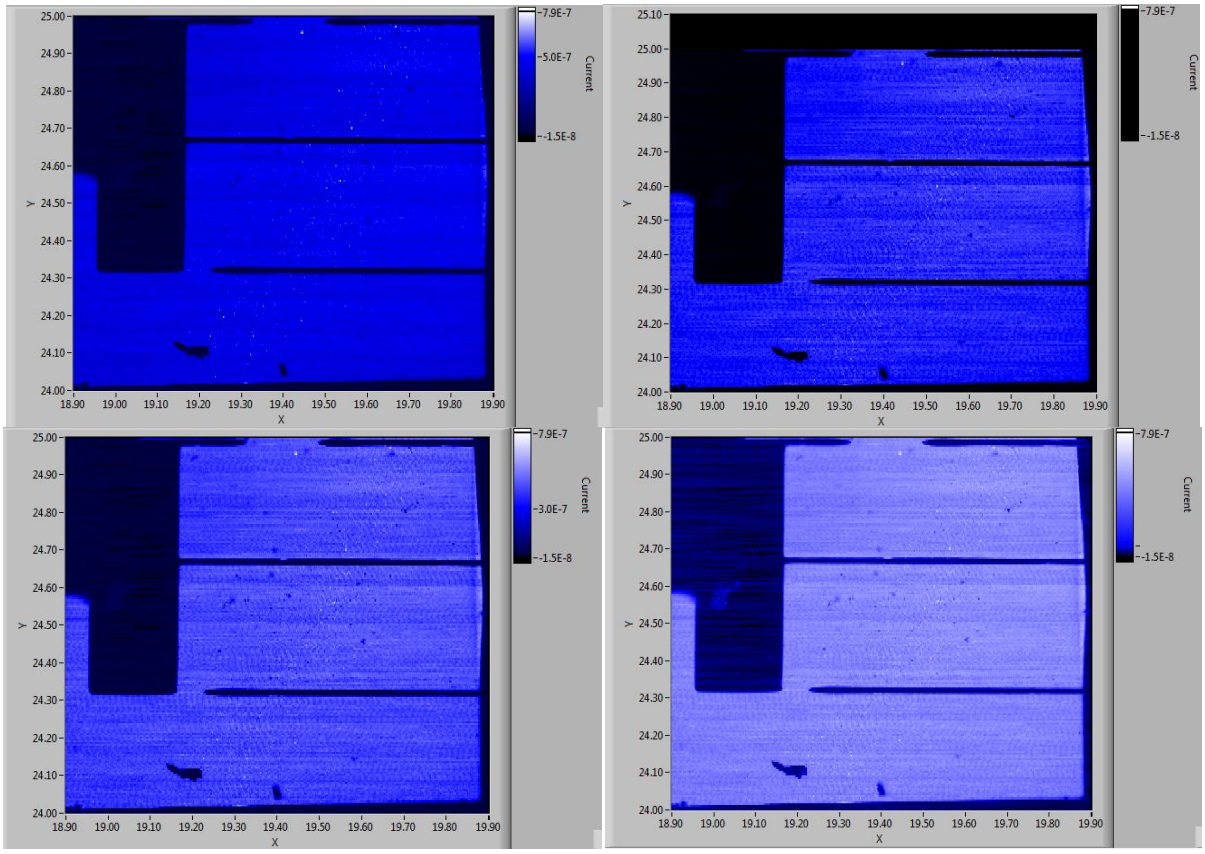

Fig. 33 - Colour-scaling affects conclusions drawn from visual analysis of PC maps

Before proceeding further, it is useful to mention that all PC maps should be treated carefully before making conclusions based on them. Fig. 33 demonstrates the profound effect that scaling the colour-map representation of the current signal has on the ability to resolve features from a scan. One can 'scale' the signal by choosing the current amplitude on which to centre the boundaries between light and dark colours on the PC map. Thus, one can bias the colour scaling in the maps to bring out local points of higher current or local points of lower current. The whole colour scale can also be shifted to emphasize phenomena that only occur at particular current levels e.g. nano-Amp noise fluctuations. Images serve as a fast and very important way to discern information from obvious features in PC scans, but ultimately, more rigorous analysis can be performed on the raw data in order to quantify conclusions based on PC mapping.

6.2 Orthogonal Scans

The long strips displayed in Fig. 34 are three different scans of the same region, and were originally scans for analysis of the ITO sheet resistivity by analysing PC across the metal fingers.

The two PC maps (a) and (b) of Fig. 34 have been rotated anticlockwise by 90°, but were originally taken such that rastering line scans begin from the bottom of each strip and end at the top. The PC map in Fig. 34 (c) is of the same area except double as thick, and was scanned with lines from left to right.

There are two major points of interest – these scans show that streaking noise is purely confined to the scan direction.

Moreover, in the area denoted by the red oval, there is a very faint signal which corresponds to a scar which is one NW in thickness. Importantly, the scar only shows up in the PC maps (a) and (b) where line scans cross roughly perpendicular to the one-dimensional feature. The reason that such a feature may not be resolved in the scan (c) parallel to the feature is that choosing too few pixels for the domain in the vertical dimension of (c) might leave gaps between scan lines when the rastering program runs. Since the feature is so thin, not all vacancies in the NW array corresponding to the scar are recorded in the PC data, and thus it does not show up in the PC map.

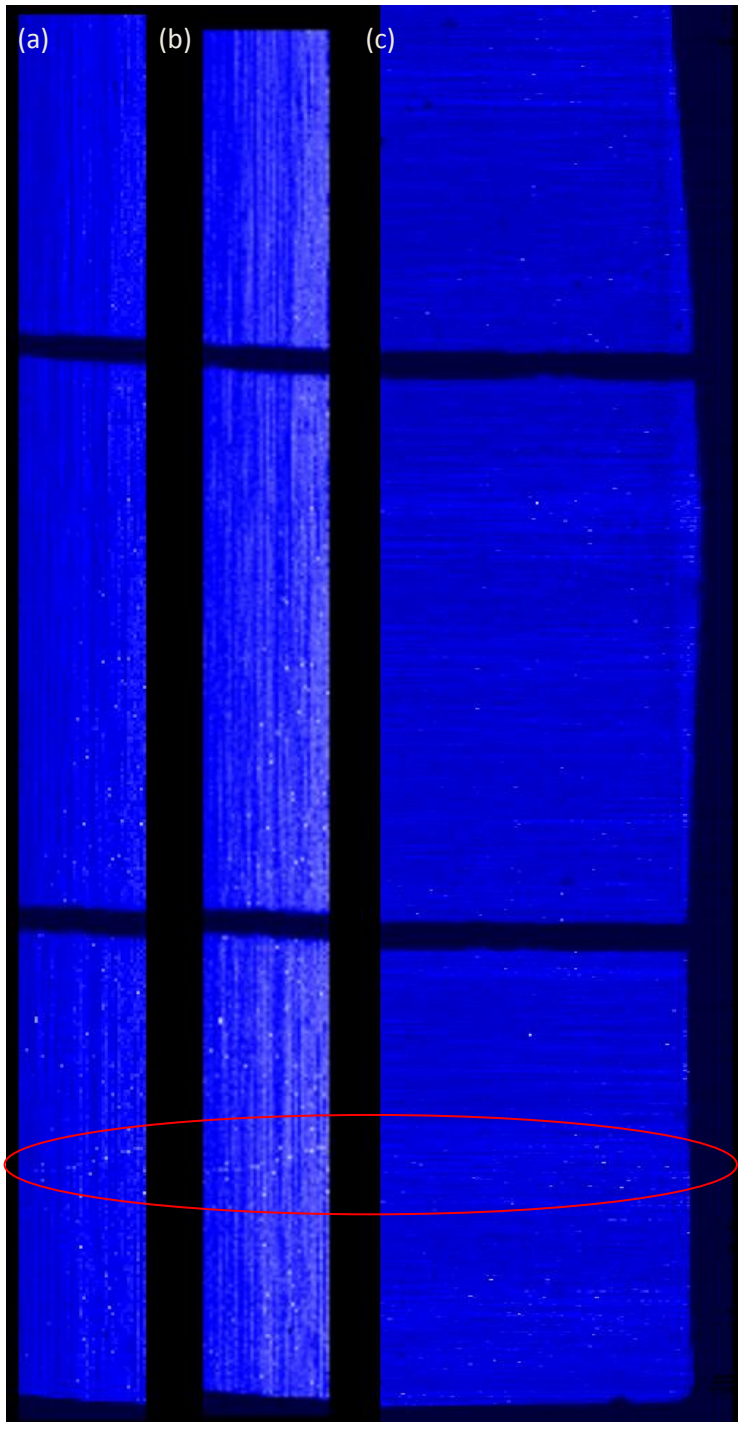

Fig. 34 - Three scans of the same region

6.3 Broken Nanowires & NW Vacancies

After refinement of the technique, PC maps of a very high resolution were achieved, resolving features of down to ~800nm in size.

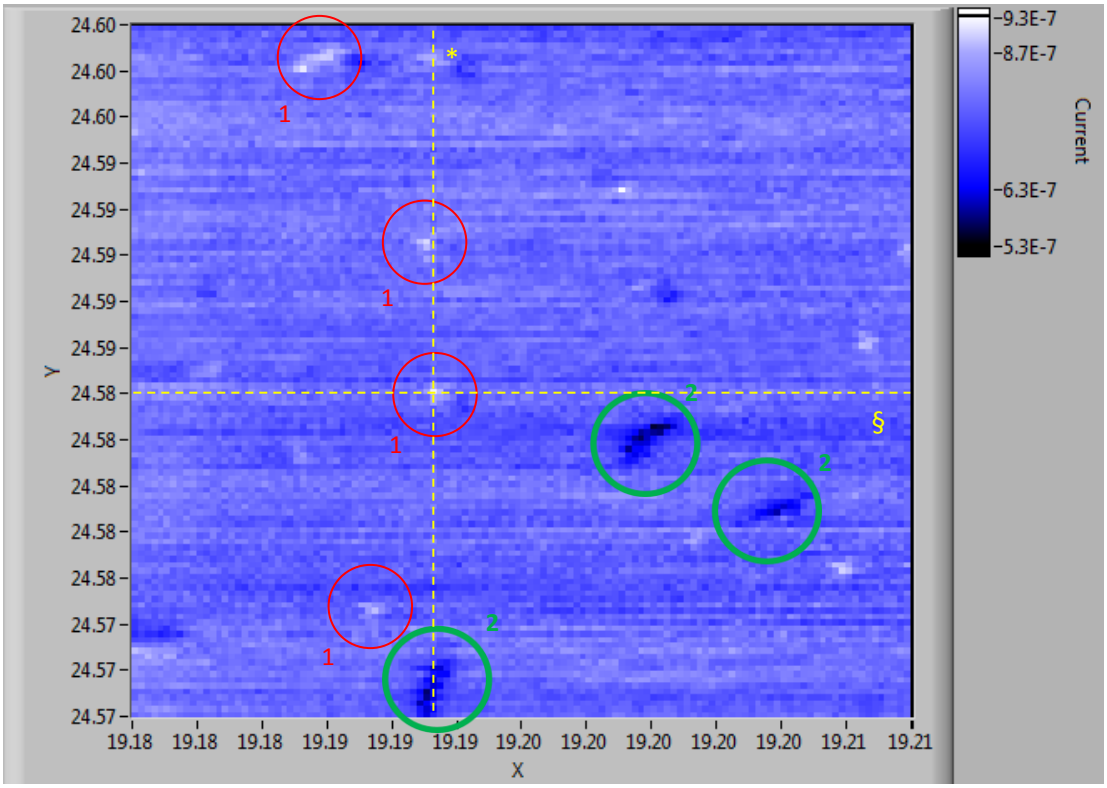

Fig. 35 - PC map indicating missing and broken NWs

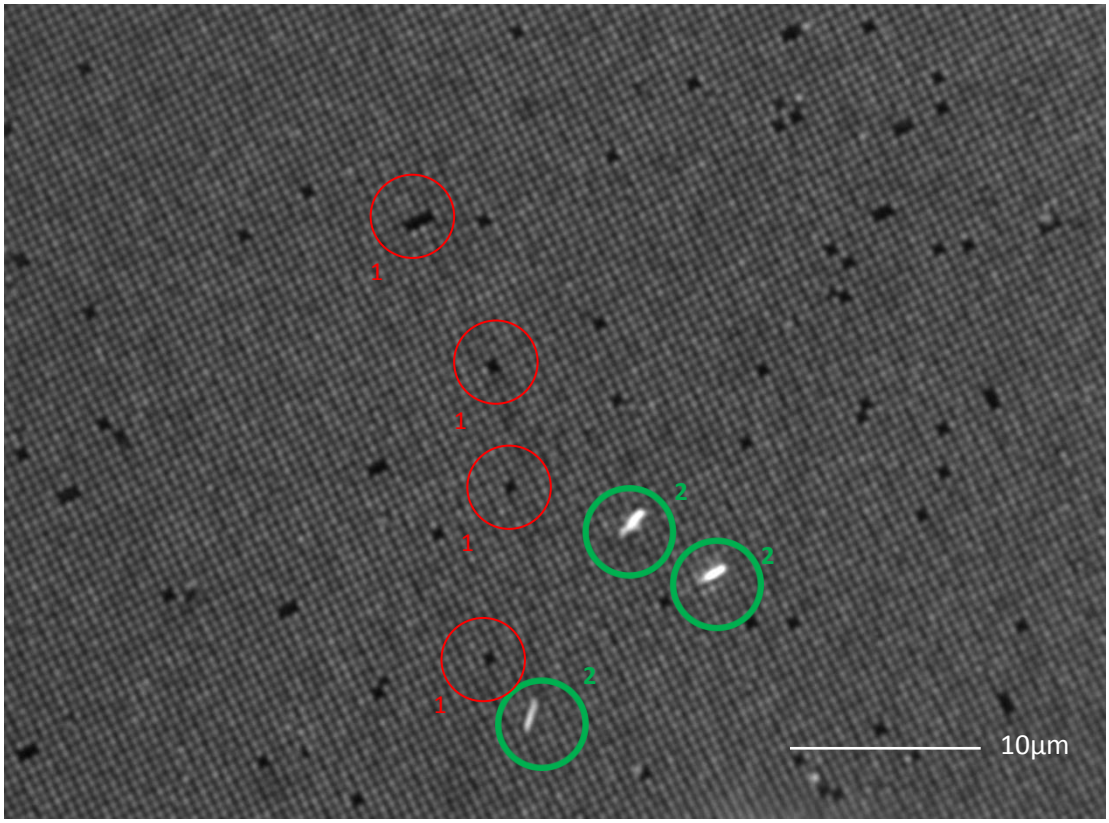

Fig. 36 - Camera image indicating missing and broken NWs

Fig. 35 & Fig. 36 show vacancies in the NW array where NWs are missing – indicated by red circles (1) and short segments of broken NWs lying on the surface indicated by green circles (2). This is an important result, showing that the scanning PC technique has been able to resolve small features at high resolution. Moreover, the PC map relates the features to their effect on the current signal.

The broken NWs lying on the surface of the active NW array show up as dark spots on the PC map. This falls in line with expectations that the disconnected broken NWs shadow the active area of the device, limiting current generation underneath them. From an analysis of the entire current map data, the minimum current generated is 5.5 x 10^{-7}A underneath the broken NW at (x,y) = (19.19, 24.7). This shows that broken NWs laying on the surface do not reduce the PC to zero as do other features such as metal contacts (see Fig. 32). The reduced current corresponds to a level equal to 70% of the average current over the entire PC map.

However, Fig. 35 & Fig. 36 also contain a surprising result. Points in the NW array where a NW is missing, broken or imperfectly grown result in increased current generation, as evidenced by the PC map. The result is puzzling, as a missing NW would ostensibly indicate the absence of a p-n junction. Thus one would expect a decrease in current generation at these points. [16] and [26] seem to support this notion, as those studies indicated regions of lower current generation between adjacent NWs where a p-n junction is lacking. However, the situation here is slightly different because the exposed pits corresponding to missing or broken NWs in this case should have different characteristics to the spaces in between NWs in those papers, which are regions without p-n junctions consisting simply of a substrate coated with an insulating layer.

6.4 Investigation of High-Current NW Vacancies

The surprising result warranted further investigation. To begin with, I analysed the current signal to determine the magnitude of the current increase in regions corresponding to NW vacancies. Fig. 37 shows a vertical line profile of the current signal, corresponding to the line (*) in Fig. 35.

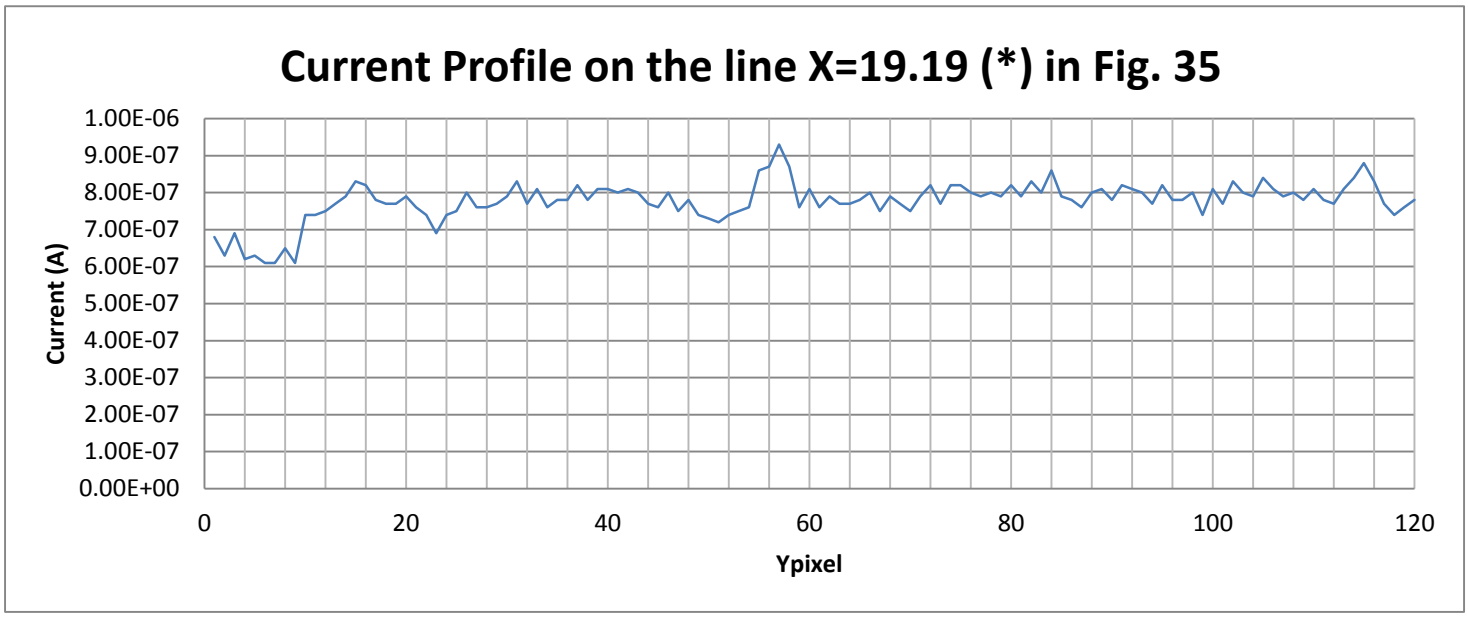

Fig. 37 - Profile of current signal along the line X = 19.19 (*) in Fig. 35

A horizontal profile of the current signal indicated by the line marked (§) in Fig. 35 is shown in Fig. 38. Firstly, it is important to note the greater homogeneity of the current signal in Fig. 38. This is due to the shorter time range of the data represented in Fig. 38 as it corresponds to a horizontal line scan which in this case takes roughly five seconds, whereas the data represented in Fig. 37 displays

data ranging in collection time from the start to the end of the PC scan which takes roughly twelve minutes. Thus, further analysis of the single NW vacancies will be restricted to horizontal line scans taken individually, as these are independent of large long time-scale variations in the current which have been interpreted as noise (as discussed in section 6.5).

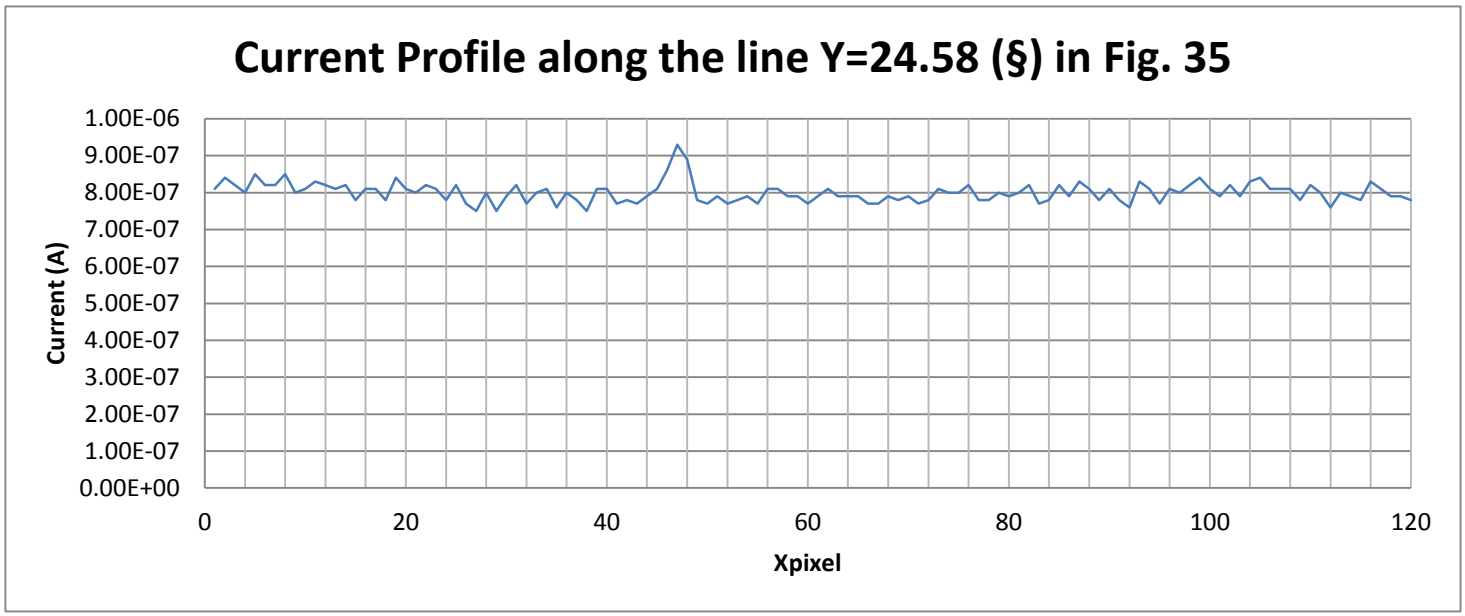

Fig. 38 - Profile of current signal along the line Y = 24.58 (§) in Fig. 35

Analysis of the NW vacancy situated at the intersection of the two current profiles in Fig. 35 is presented here. The current corresponding to the NW vacancy reaches 9.3×10^{-7}A which is also the peak current over the entire PC map. As mentioned previously, the most reliable interpretation of the current signal is achieved if one restricts analysis to a single line scan. With this restriction, the peak current corresponding to a NW vacancy is 16.6% greater than the average current level of 7.98×10^{-7}A over the profile presented in Fig. 38 (where the peak current and surrounding two data points are excluded from the average as this gives an indication of the magnitude of the current produced from a NW vacancy, relative to the current produced by a uniform NW array). The difference between peak current and average current is 1.32×10^{-7}A.

Following this analysis, I scanned a larger pit of 6µm diameter to investigate whether the high-current phenomenon is strictly observed in NW vacancies of ~870nm in diameter. The pit is the same one indicated by the red circle (5) in Fig. 30 & Fig. 31. The resultant PC map is shown in Fig. 39 below.

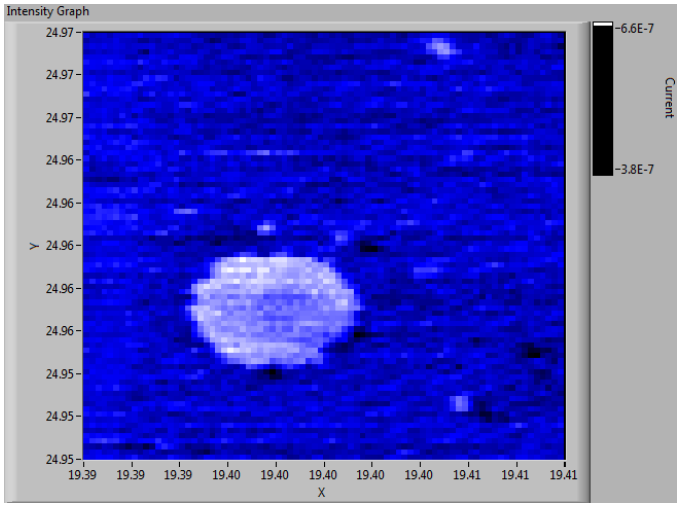

Fig. 39 - PC map of a large pit with diameter 6µm consisting of multiple NW vacancies

Clearly, a large pit similarly produces increased PC compared to the surrounding uniform NW array. Firstly, it should be noted that the pit seems to be caused by processing, and not handling damage. This is inferred from its particularly round shape, lack of visible damage indicators, and the presence of a few identical large pits on other parts of the sample.

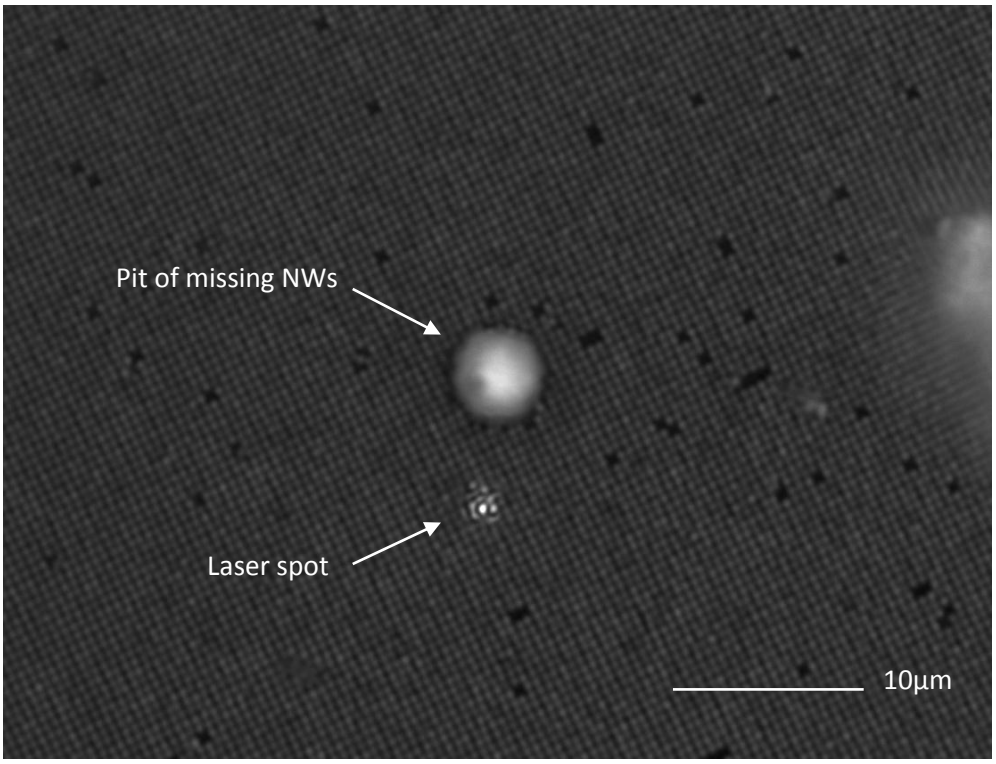

Fig. 40 - Camera image of a large pit ~12 NWs (6µm) in diameter

Fig. 40 is a camera image of the pit, and demonstrates its size relative to surrounding NW vacancies. The bright spot below the pit is the laser which has been tightly focused and passed through the strongest intensity filter in order to isolate the intensity peak. Fig. 41 is a camera image which shows unidentified features distributed irregularly over the base of the pit. A rudimentary analysis of Fig. 39 shows the maximum current from the pit to be 6.60×10^{-7}A which is 32% higher than the 4.99×10^{-7}A current averaged over the entire PC map. This represents a significant increase in photocurrent.

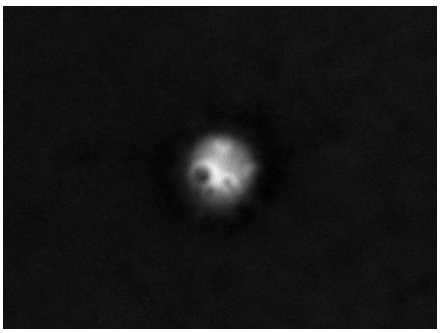

Fig. 41 - Large pit imaged at the base

The pit was scanned repeatedly with the laser at different intensities, and imaged to a spot with the focal plane at the height of the NW array surface as in (b) of Fig. 43, and then at the base of the pit as in (a) of Fig. 43. This was performed in order to investigate whether the high current signal from the pit could be related to optical effects. For instance, leaving the focal plane at the height of the NW array surface might cause the diverging cone of radiation reflected from the base of the pit to interact with several NWs at the edge of the pit (see (b) of Fig. 43); or perhaps a gold particle left at the bottom of the pit might scatter radiation towards nearby NWs and similarly result in higher than expected photocurrent. The resultant PC maps from these scans are shown in Fig. 42. All scans show increased PC in the pit. Notably, compared to the high intensity setting used in Fig. 39, reducing the intensity progressively from scan (1) to (2) in Fig. 42 increased the relative noise level, ultimately leading to a highly obscured PC map.

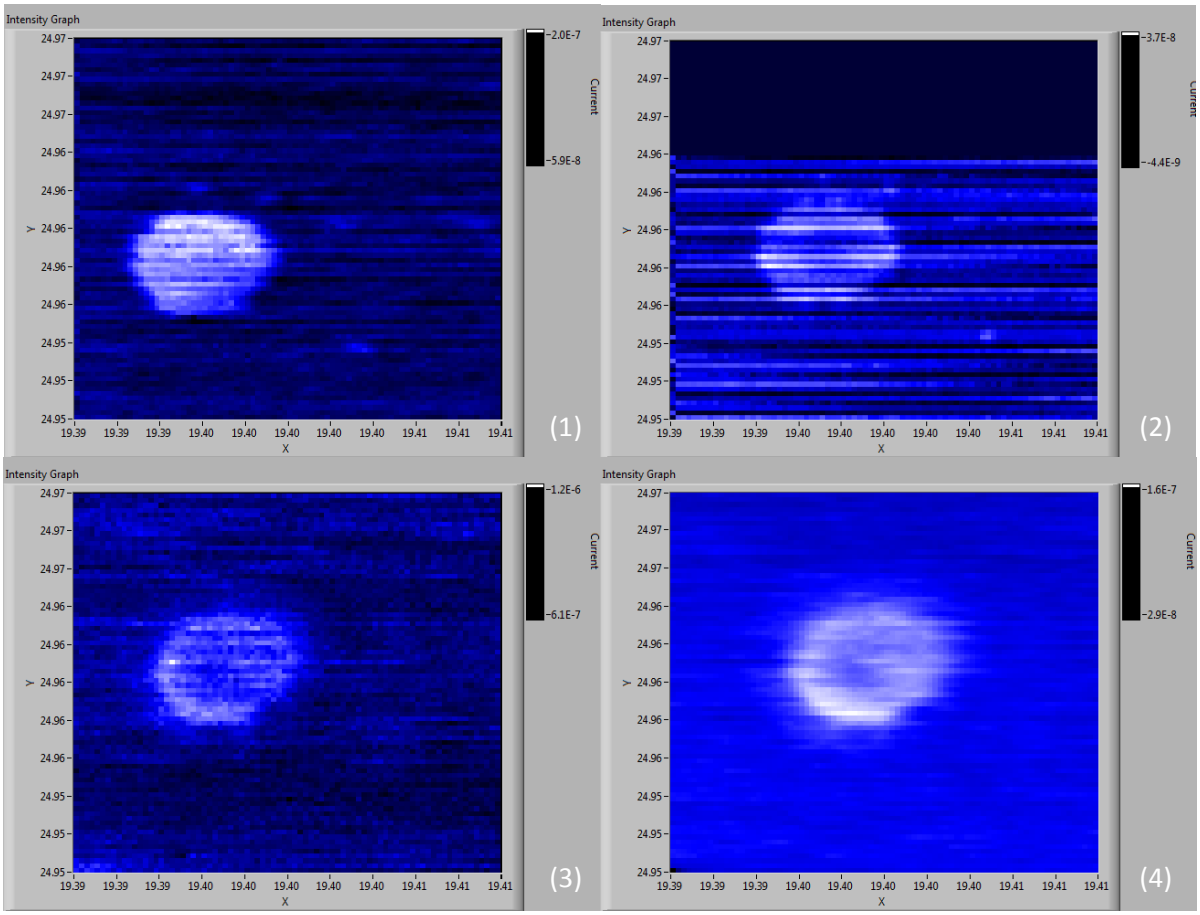

Fig. 42 - Pit scanned with varying intensity and focal depth: (1) focal plane at NW array surface, medium intensity; (2) focused at NW array surface, lowest intensity; (3) focused at pit base, high intensity; (4) focused at pit base, low intensity

One can observe in Fig. 42 that the effect of focusing the laser beam to the base of the pit as in scans (3) and (4) was to reduce the resolution of the PC map in the region outside the pit. Small features in the surrounding NW array such as lighter coloured dots representing NW vacancies are observable when the laser is focused at the height of the NW array surface as in Fig. 39 or scans (1) and (2) of Fig. 42 but are not visible in scans (3) and (4). This could be the expression of an effect similar to that explained below in section 6.8 whereby a step change in the height of the surface topography causes the features of interest to intersect the cone of laser radiation above the focal plane, such that the laser is imaged to a larger spot, reducing the resolution of the resultant PC map.

Moreover, comparing scan (3) of Fig. 42 with scan (1) demonstrates that focusing the laser beam to the base of the pit reduced the relative increase in PC observed in the pit when compared to the surrounding NW array. The reduction in PC is greater at the centre of the pit than at the edges. A credible hypothesis is that specular reflection of the laser radiation from the bottom of the pit occurs in a manner more similar to (a) of Fig. 43 such that a greater portion of the reflected cone of radiation escapes from the pit without interacting with NWs at its edge, particularly as the laser scans across the centre of the pit. This effect could be significant due to the high numerical aperture of the 100x objective focusing the beam to a cone with a wide opening angle of 106.26° at the focal plane.

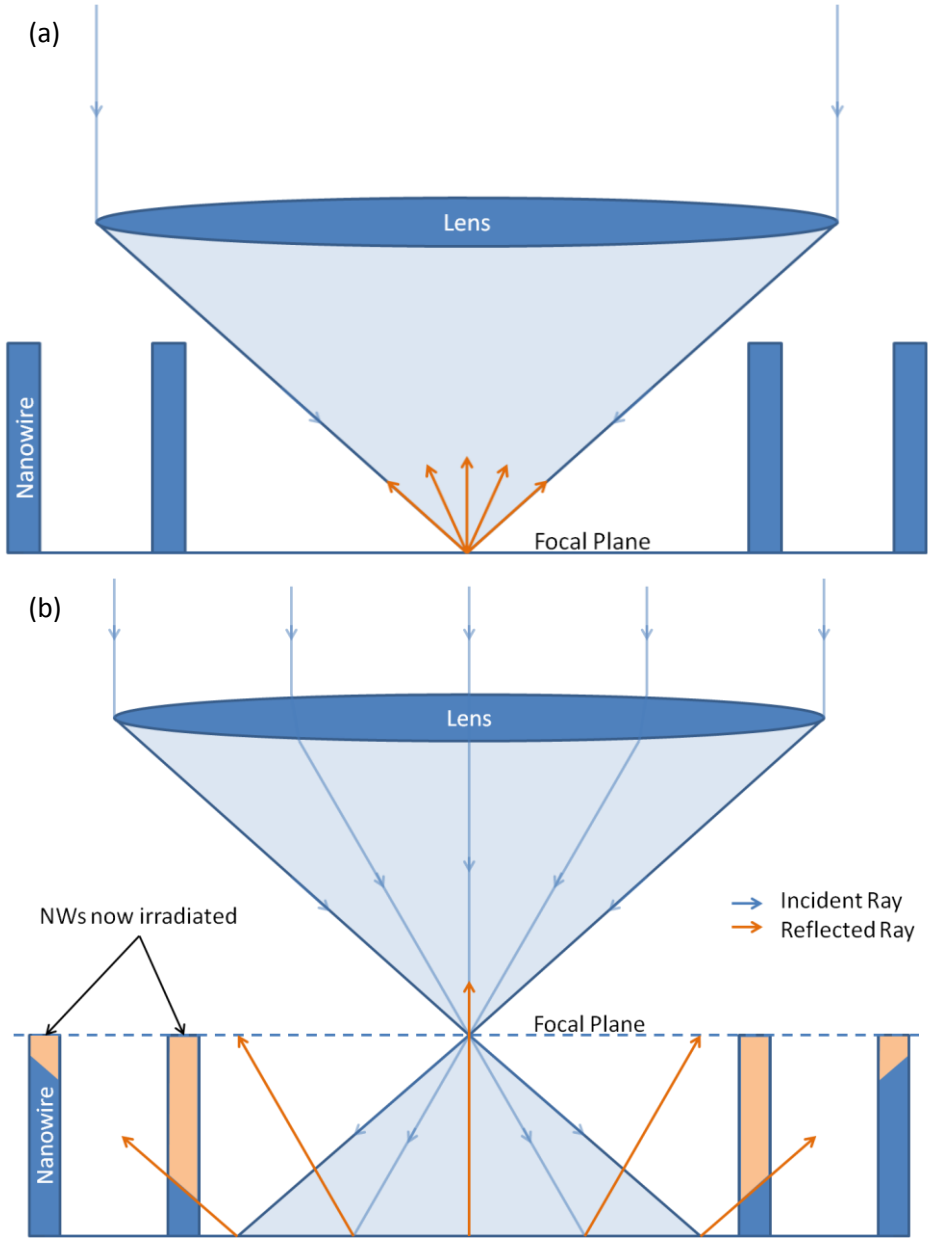

Fig. 43 - (a) Cone of laser radiation focused at the base of the pit enters and exits without irradiating surrounding NWs; (b) Laser focused at the NW surface may irradiate surrounding NWs to produce higher than expected photocurrent

Nevertheless, it is clear that NW vacancies result in increased photocurrent for both large and small holes.

A final investigation into the NW vacancies revealed that they could be caused by processing, and not by damage as at first thought. Fig. 44 shows a PC map of the thin, green semi-transparent layer on top of the NW array, as marked by the green circle (2) in Fig. 30. The higher-resolution scan clearly shows that very little current is generated from areas underneath the layer. Of particular importance is that while NW vacancies exist outside the region covered by the layer and exhibit the high-photocurrent phenomenon, similar vacancies underneath the layer (visible in the camera image on the right in Fig. 44) do not. This indicates that the vacancies are not caused by handling damage – no holes have penetrated through the layer. Rather, the vacancies existed before deposition of the layer, and are thus most likely caused during processing.

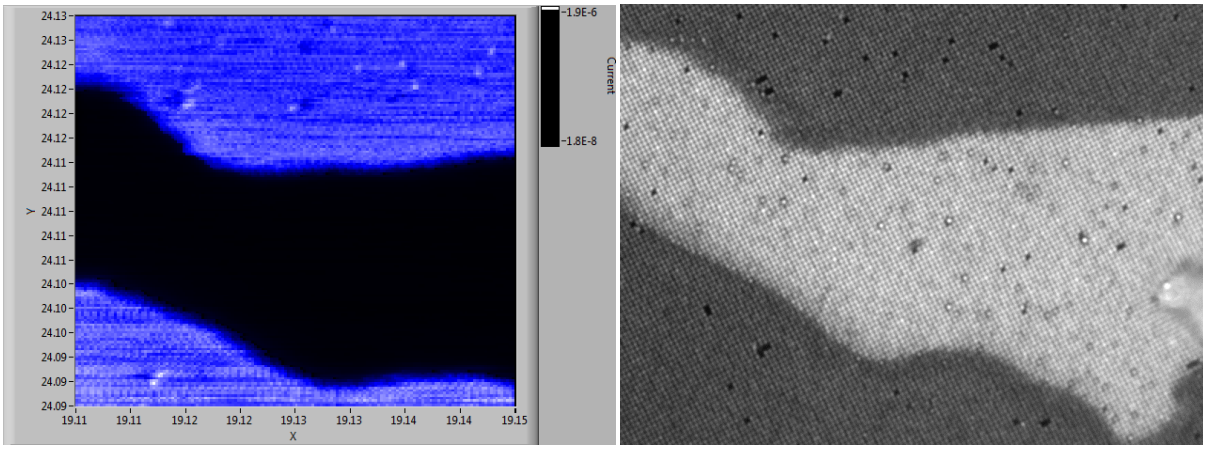

Fig. 44 - Green coloured masking layer – (left) PC map, (right) camera image

Interestingly, the layer is strongly reflective of green light, indicated by the green colour observed through the ocular. Since some sort of patterning underneath the layer is visible under broadband illumination as evidenced by the camera image, perhaps with PC spectroscopy scans of the device, a different resultant PC map might be obtained with regard to this feature.

The exact cause of the NW vacancies remains undetermined. The missing wires could be caused by inhomogeneous distribution of metal seeds during the nano-imprint lithography stage. Alternatively, perhaps NW vacancies occur after the device begins operation – since the NW array consists of multiple p-n junctions in parallel, NWs with lower V_{OC} than the surrounding array act as shunt paths and may experience high levels of current resulting in destruction of the p-n junction similar to hot-spot heating in PV modules. In any case, the NW vacancies and their associated high-photocurrent phenomenon should be further investigated to determine the cause of the vacancies and the mechanism of high current generation, potentially opening a pathway to more efficient devices.

6.5 Noise Analysis & Signal-Noise-Ratio

As mentioned previously, even the clearest photocurrent scans exhibit high levels of noise and artefacts, obscuring the PC signal and limiting the amount of useful information that can be deduced from PC scans. In order to quantify the level of noise, analysis was performed and a signal-noise ratio was determined.

Firstly, it is important to recall the different types of noise that exhibit themselves in the PC scans. ‘Streaking’ refers to single horizontal lines of a constant current level that occur over time scales of roughly one line scan (the duration can vary, depending on input parameters). ‘Banding’ refers to a similar phenomenon which exhibits itself over a longer time scale, resulting in bands of horizontal lines with sustained higher or lower current. Finally, ‘artefacts’ refer to systematic errors or patterns in PC maps caused by the measurement apparatus itself.

To determine the source of the noise, scans were performed in order to remove potential sources one by one, and to analyse the effect on the current signal. Firstly a scan was performed with lights off, and the laser was set to irradiate a homogeneous active area of the device, with the stage switched off to eliminate movement of the sample. Thereafter, the laser was switched off, and another scan was performed in which only ambient light and the electrometer could be isolated as sources of noise.

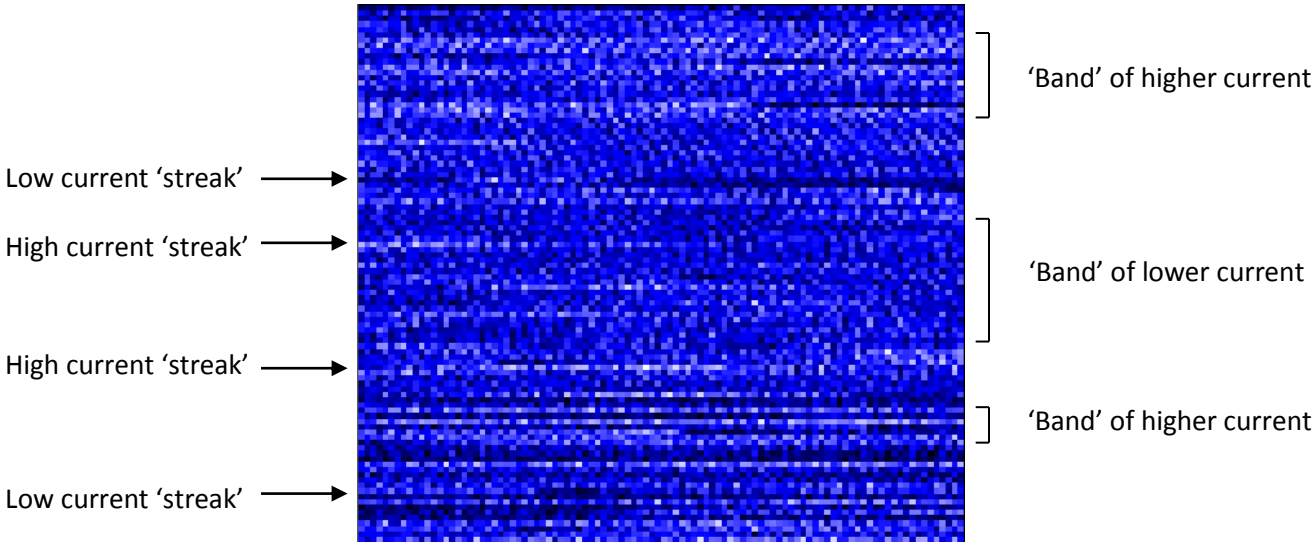

Fig. 45 - Noise scan with the laser demonstrates banding and streaking

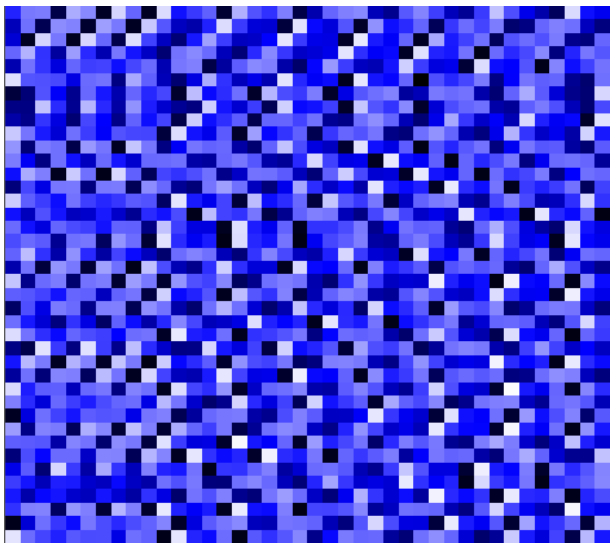

Fig. 46 - Noise scan without the laser demonstrates the diagonal artefact pattern

Fig. 45 & Fig. 46 show the results. Note the spatial dimension is meaningless in these scans, as the translation stage has been switched off. The scans merely represent the time-dependence of noise phenomena, and time increases from left to right along scan lines, and then from bottom to top, just as in all previous rastered scans (refer to Fig. 13 for an illustration of the temporal progression).

It is clear that the laser is the source of banding and streaking, as without the laser, there is no evidence of these noise phenomena. This noise is most likely an expression of a pulsating laser which increases and decreases in intensity over longer time scales.

Fig. 46 indicates that the diagonal artefact visible in all PC maps originates in the electrometer/software interface. Interestingly, the diagonal artefact appears not only without the laser, but also in scans with the laser. This suggests that it results from the electrometer circuitry, and is amplified along with the signal e.g. when the electrometer receives a higher current input due to higher PC from the solar cell.

To quantify the effects of these noise sources on scans, I analysed the output from noise scans such as those in Fig. 45 & Fig. 46, and compared them to scans of the NW array device performed immediately thereafter. As seen in Fig. 32, the amplitude of the signal related to non-laser based

current fluctuations is very small. Taking the range over the PC map in Fig. 46, one arrives at maximum peak-to-trough current amplitude of 4×10^{-9}A. Of course, the minimum reference around which this signal is centred differs from one scan to the next, depending on how the electrometer has been calibrated. Nevertheless, it is obvious that the electrometer-based current fluctuation in the absence of irradiation is small.

To arrive at a sensible estimate of the short-time-scale noise signal under laser irradiation, the range in current magnitude was extracted from each horizontal line in a noise scan similar to Fig. 45 (wherein the stage is switched off, but the laser irradiates a homogeneous region of the cell). The average value of these ranges was then calculated, and this figure was used as the mean peak-to-trough current fluctuation for horizontal line scans due to an oscillating noise signal from the combination of the laser and electrometer. The value represents the peak-to-trough current fluctuation that one could expect to see in horizontal line scans such as Fig. 38 which is purely derived from noise. This value was 9.80×10^{-8}A for the noise scan conducted immediately before taking the PC scan referred to in Fig. 35 through to Fig. 38, and is more than twenty times higher than the peak-to-trough noise signal amplitude from the electrometer alone.

A similar calculation was performed to estimate the long-time-scale noise signal due to a pulsating laser. This time, however, the range in signal level from each vertical line was taken, and the resultant peak-to-trough amplitudes were averaged to yield a figure of 1.16×10^{-7}A. This figure gives an estimate of the maximum to minimum current variation that one could expect to see in vertical line scans such as Fig. 37, and is indicative of the effect of 'streaking' and 'banding' on the PC maps. It is 20% higher than the peak-to-trough current oscillation found in horizontal lines.

Finally, the signal-noise-ratio (SNR) was determined for the scan in Fig. 35 which was performed immediately after the noise scan. The Signal-Noise-Ratio was defined by the formula:

$$SNR = \left(\frac{A_{SIGNAL}}{A_{NOISE}}\right)$$

where A_{SIGNAL} is the maximum amplitude of signal fluctuation in a horizontal line scan from a real photocurrent map[34], and A_{NOISE} is the amplitude of the short-time-scale noise signal under laser irradiation determined from a noise scan as above. This ratio is of particular interest, as the wavelength of the current signal fluctuation in the case in Fig. 35 is on a length scale which could indicate the resolution of individual NWs.

The SNR for Fig. 35 was 1.45, which is very low. This indicates that any observed current fluctuations within horizontal lines in Fig. 35 are almost indistinguishable from expected noise. Thus, it is difficult to infer that observed current oscillations are evidence for physical characteristics such as the presence of individual NWs.

For similar reasons, the high noise level of the apparatus in its current state prohibits measurements such as ITO sheet resistivity measurements, which show up as small gradual changes in current, and would thus be heavily masked by the noise signal. Although frequency analysis could be performed in an attempt to subtract the noise signal, this would prove difficult due to the irregularity in the frequency of the larger sources of noise.

[34] Determined by the same process as the 'short-time-scale noise signal' above

6.6 Spot Size

The spot size is one of the key determinants of the spatial resolution for the spatially-resolved photocurrent microscopy technique. Thus, attaining a small spot size is of great interest. Low-resolution scans are easy to achieve, requiring only loose constraints on the spot size. The highest possible spatial resolution however can be limited by spot size via one of two mechanisms: the size of the aperture, or the diffraction limit defined by the microscope objective.

If determined by the size of the aperture through which the laser beam is focused, a simple calculation reveals that the achievable spot diameter is 180nm based on the focal lengths of the apparatus.

$$Spot = 5\mu m \cdot \frac{1.8}{50}$$

The more limiting condition on the spot diameter is found to be the diffraction limit of the microscope objective:

$$\delta x \approx \frac{\lambda}{2NA}$$

where *NA* is the numerical aperture of the objective. With laser of wavelength 532nm, and 100x objective with *NA* = 0.8, this yields a diffraction limited spot diameter of 332.5nm.

Thus the spot diameter is diffraction-limited to 332.5nm.

However, it is also important to note that the absolute diameter of the spot is not the only factor that limits the spatial resolution of the scanning photocurrent technique. As discussed in [31], the intensity profile of the spot can be distributed such that the highest intensity portion of the beam is confined to a region smaller than the spot diameter. This is illustrated in Fig. 47 & Fig. 48.

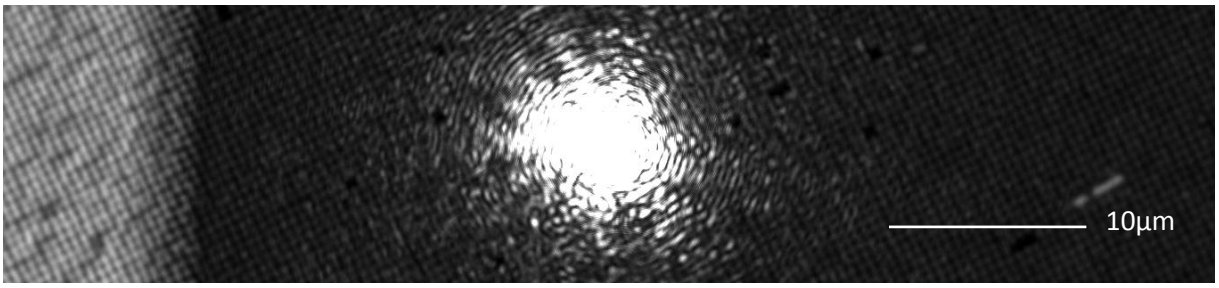

Fig. 47 - Apparent spot size with high laser intensity (intensity filter on minimum setting)

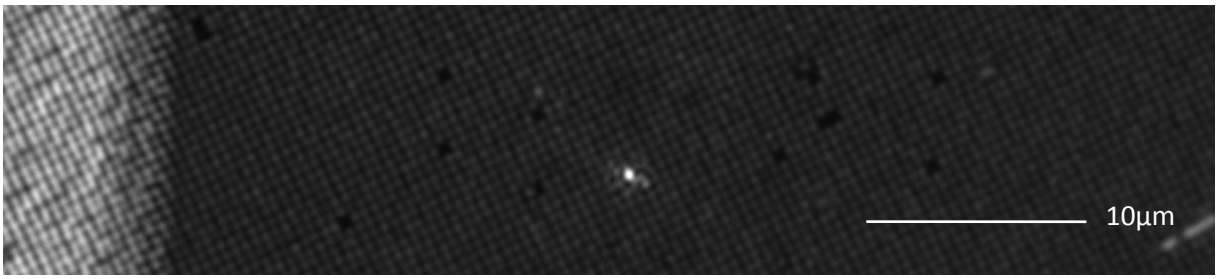

Fig. 48 - Apparent spot size with low laser intensity (intensity filter on maximum setting)

In Fig. 47, a moderately exposed camera image of the spot at the high intensity setting suggests that it is quite large and certainly not confined to a size that would allow resolution of individual NWs. However, upon isolating the intensity peak of the laser spot by increasing the intensity filter

setting and decreasing the camera exposure time, it is observable in Fig. 48 that the intensity peak is in fact confined to a spot with a diameter on the order of the NW pitch.

6.7 Spatial Resolution

Spatial resolution refers to the physical size of the smallest feature one can make out in a photocurrent map based on the limitations of the apparatus. Higher resolution implies smaller discernable features. With sufficient spatial resolution, this laser-based photocurrent mapping technique has the potential to resolve individual NWs. This could allow one to determine, for example, whether a significant proportion of NWs are poorly contacted, to analyse variation in V_{OC} and I_{SC} over the array, and to determine whether the majority of the NW array is limited by one poorly performing NW.

Ultimately, the spatial resolution of the scanning photocurrent microscopy technique is determined by a number of factors – it could be limited by the step-size of the nanomover which allows 10nm/step increments; the minimum parameters (e.g. pixel size) one can choose before the nanomover's speed falls below its 5µm/s limit; and the minimum spot size determined above.

For this apparatus, the maximum spatial resolution is defined by the diffraction-limited spot size of 332.5nm. This is still less than the 500nm NW pitch, indicating that one should be able to resolve individual NWs with this apparatus. The conclusion is that noise, not spatial resolution is the factor which prohibits the identification of individual NWs in the photocurrent maps.

6.8 Defocusing Induced by an Inclined Surface

One of the significant limitations to the apparatus in its current state is the difficulty with which one can control the sample's tilt angle with respect to the microscope's focal plane when mounting the chip to the carrier. This gives rise to the major problem whereby scanning the laser over a tilted sample results in defocusing of the spot as the laser moves away from the point where it was focused, resulting in varying resolution over a single scan. The same effect occurs if the surface topography of the cell is slanted such that it is not aligned with the microscope's focal plane, even if the sample has been mounted correctly. Fig. 49 illustrates the defocusing problem.

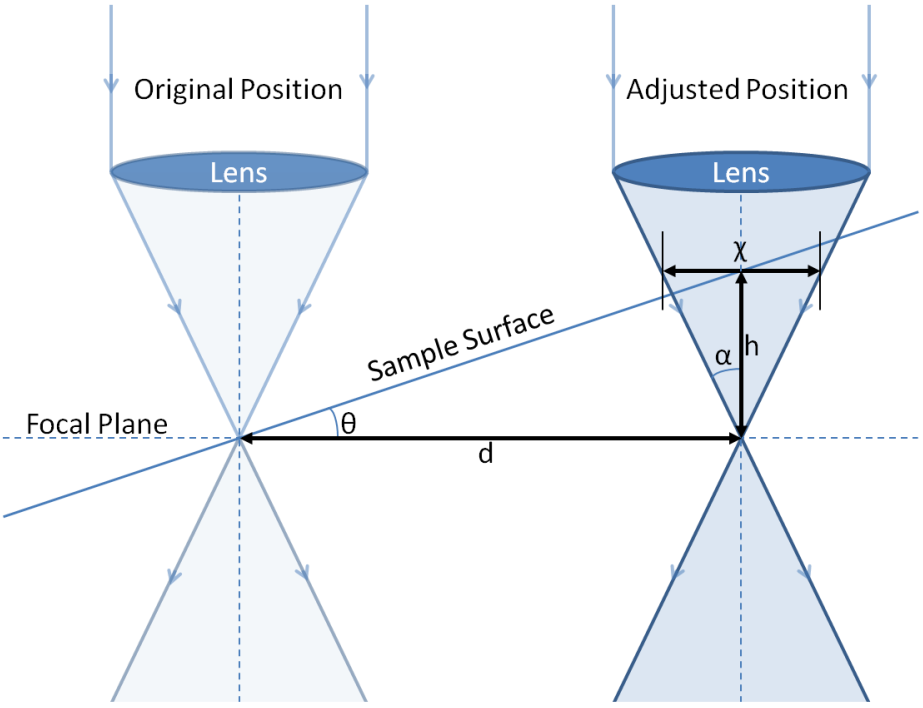

Fig. 49 - Geometric illustration of variation in spot size due to an inclined sample surface

A relationship between the approximate diameter x of the spot after the laser has scanned a distance d away from its initial focal point gives an idea of the loss in resolution which occurs due to a tilted sample. For a sample inclined at tilt angle θ with respect to the microscope's focal plane, and taking x as a good estimate for the spot size (which is true for small θ); by geometry:

$$\tan\theta = \frac{h}{d}$$

$$h = d\tan\theta$$

Where h is the elevation of the sample surface above the focal plane at the newly adjusted position of the laser spot. Also by geometry:

$$\tan\alpha = \frac{x}{2}\cdot\frac{1}{h}$$

Where α is the half-angle of the maximum cone of light exiting the microscope objective. Substituting the expression for h:

$$\tan\alpha = \frac{x}{2d\tan\theta}$$

One finally arrives at the expression:

$$x = 2d\tan\alpha\tan\theta$$

$$\text{for } 0° < \alpha < 90° \text{ and } 0° < \theta < 90° \text{ and } \theta \to 0°$$

This expression indicates that the spot will always defocus as the laser scans across the surface of a tilted sample. The effect will be greater for longer scan domains, larger tilt angles and for higher numerical apertures. A microscope's numerical aperture is given by the relation:

$$NA = n\cdot\sin\alpha$$

Where the refractive index $n = 1.0$ in air:

$$NA = \sin\alpha$$

For the given objective's numerical aperture of 0.8:

$$\alpha = \sin^{-1}0.8 = 53.13°$$

When the sample is at a relatively large tilt angle $\theta = 5°$, the change in spot diameter per unit the laser scans along the focal plane is given by:

$$x = 0.23d$$

Consider as an example the scan of the whole cell in Fig. 27 which involved scanning over a large domain 1mm wide. Since the laser spot was focused at the centre of the cell, then an estimate of the spot diameter at the edge of the cell is given by:

$$x = 0.23\cdot 500\mu m = 116.65\mu m$$

Such defocusing is significant – the diameter of the defocused spot at the edge of the scan domain is two orders of magnitudes greater than the optimum diffraction-limited spot diameter of

332.5nm as determined in section 6.6. This implies a corresponding decline in resolution of two orders of magnitude.

Moreover, tilting may occur in each of the two dimensions perpendicular to the focal plane. This exacerbates the problem of controlling the tilt angle of the sample such that it is perfectly coplanar with the microscope's focal plane. Ultimately, the approach I took to counter this problem involved firstly propping up the sample with small tabs of paper until there was as little focal variation as possible over the 1mm x 1mm domain I was interested in scanning. At the beginning of each scan, I would then focus the laser at the centre of the feature I was investigating. This would ensure that the laser would resolve the feature even if the focal point was below the sample surface on one side of the feature and above the sample surface on the other. On particularly large scans, it was necessary to monitor the spot size over the duration of the scan and to adjust the focus accordingly.

7 Conclusions & Outlook

The scanning photocurrent microscopy technique developed in this thesis has proven that it can spatially resolve the photocurrent from a NW array solar cell, and furthermore that its application to NW array PV cells is fast and accurate, and can provide useful information on factors that affect cell efficiency. The technique in its current form, however, is not without limitations – particularly the existence of substantial laser-induced noise in the photocurrent signal and resolution lost due to sample tilt. Should these limitations be addressed and the apparatus upgraded, it has the potential to provide significant information on the unique photovoltaic properties of NW array solar cells by taking, for example, highly spatially-resolved quantum efficiency measurements.

The technique has been shown to accurately resolve features on a NW array solar cell by comparing photocurrent maps with camera images of corresponding regions. It resolved large features including processing defects – incomplete fingers and an opaque layer deposited on top of the ITO – which reduced the current output from regions of the cell beneath them. Another region at the right edge of the sample device was shown to generate high photocurrent when mapped, and demonstrated that these large features affect the current signal in different ways. The technique also proved capable of resolving small features in the photocurrent signal, achieving a spatial resolution of at least ~800nm when mapping the photocurrent from vacancies in the NW array. Of particular interest is the surprising result that photocurrent measured at vacancies in the NW array was consistently higher than over the surrounding uniform array.

The technique was particularly successful at identifying opaque features (e.g. metal contacts, a green layer deposited on the ITO, broken NWs) which strongly affect the PC signal by way of interacting with the laser beam before absorption of radiation in the p-n junction. However, the apparatus in its current state has been unable to provide information on characteristics measured as weaker fluctuations or gradients in the current signal (e.g. ITO sheet resistivity, or other minor changes in current across the array that could result from non-uniform processing). The reason is that the noise level is too high to make meaningful interpretations from the produced PC maps. Noise analysis revealed that an unstable laser and artefacts originating in the electrometer-software interface are probably the cause, yielding noise significant enough to make analysis of low-amplitude signal fluctuations difficult.

The accurate mapping of single NW vacancies confirmed that the apparatus was capable of producing photocurrent maps at very high resolution. Nevertheless, identification of individual NWs via the photocurrent map was not achieved, nor was it possible to determine the electrical characteristics of individual nanowires. Limiting factors once again included noise from the laser and artefacts from the electrometer-software interface. The additional problem of the spot defocusing as

it scans over an inclined surface constitutes a further limit to the spatial resolution of the technique. Calculations show that the apparatus can theoretically achieve spatial resolution smaller than the NW pitch if the spot were improved to the diffraction limit of 332.5nm, indicating that photocurrent from individual nanowires can be mapped if the problems with the apparatus are improved.

Outlook

There are a few obvious improvements to the apparatus which would overcome its present limitations, improve resolution, and give it the capability for producing more meaningful results:

- Replacing the laser would remove the need for beam cleaning optics, improve the intensity profile of the spot, and ultimately allow for higher resolution PC maps to be produced. A new laser might also eliminate the banding and streaking which have been attributed to the present laser.
- Replacing the electrometer might remedy the second most obvious limitation to the PC maps; namely, the artefact that has been attributed to the electrometer-software interface.
- A more robust and reliable bonding scheme would significantly mitigate handling damage to the NW array cells and remove the bonding wire which occasionally obscures the laser beam before it reaches the cell.
- Finally, the introduction of a flat sample holder to which the chip carrier could be easily mounted, and whose tilt angle could be easily adjusted in two dimensions would eliminate the problem of resolution being lost as the laser spot scans over the surface of a tilted sample.

Further Measurements

The value in the scanning photocurrent microscopy technique is realised once measurements are made which can determine the spatial variation in electrical and photovoltaic characteristics of NW array PV cells. In this thesis, a high level of noise limited the ability to acquire such data, but should that limitation be corrected, the following measurements might become possible:

- Spectroscopy – adding a tunable laser to the apparatus would allow one to determine wavelength-dependent properties of NW-array solar cells including spectral response curves and external quantum efficiency (EQE) as a function of wavelength – EQE(λ)
- Spatially-resolved EQE measurements – [40] states that local EQE can be determined from PC maps. This is achieved by simply taking the ratio of photocurrent to beam power.
- Spatially-resolved IQE measurements – local IQE metric becomes accessible if one measures reflected radiation simultaneously to photocurrent [40].

8 References

[1] IPCC, “Renewable Energy Sources and Climate Change Mitigation,” Cambridge University Press, Cambridge, 2012.

[2] R. Pietzcker et al., “The Role of Concentrating Solar Power and Photovoltaics for Climate Protection,” Potsdam, 2009.

[3] IEA, “Technology Roadmap - Solar Photovoltaic Energy,” IEA Publications, Paris, 2010.

[4] US EIA, “International Energy Outlook 2011,” US Energy Information Administration, 2011.

[5] Wikipedia, “Predicting the timing of peak oil,” [Online]. Available: http://en.wikipedia.org/wiki/Predicting_the_timing_of_peak_oil. [Accessed 5 May 2012].

[6] G. Monbiot, “When will the oil run out?,” [Online]. Available: http://www.guardian.co.uk/business/2008/dec/15/oil-peak-energy-iea. [Accessed 28 May 2012].

[7] R. Hirsch et al., “Peaking of World Oil Production: Impacts, Mitigation and Risk Management (The Hirsch Report),” NETL, US DoE, 2005.

[8] UNSW, “ARC Photovoltaics Centre of Excellence 2010/11 Annual Report,” UNSW ARC PV Centre of Excellence, Sydney, 2011.

[9] M. Green, “The Path to 25% Silicon Solar Cell Efficiency: History of Silicon Cell Evolution,” *Progress in Photovoltaics: Research and Applications,* vol. 17, pp. 183-189, 2009.

[10] W. Shockley & H. Queisser, “ Detailed balance limit of efficiency of p-n junction solar cells,” *Journal of Applied Physics,* vol. 32, no. 3, pp. 510-519, 1961.

[11] M. Green et al., “Solar Cell Efficiency Tables (version 39),” *Progress in Photovoltaics: Research and Applications,* vol. 20, no. 1, pp. 12-20, 2011.

[12] EPIA, “Global Market Outlook for Photovoltaics Until 2016,” EPIA, Brussels, 2012.

[13] US DoE, “$1/W Photovoltaic Systems White Paper,” in *$1/W Systems: A Grand Challenge for Electricity from Solar*, Washington, DC, 2010.

[14] M. Green, “Third generation photovoltaics: Solar cells for 2020 and beyond,” *Physica E,* vol. 14, pp. 65-70, 2002.

[15] M. Borgström et al., “Nanowires with Promise for Photovoltaics,” *IEEE Journal of selected topics in Quantum Electronics,* pp. 1050-1061, 2011.

[16] G. Mariani et al., “Patterned Radial GaAs Nanopillar Solar Cells,” *NANO Letters,* vol. 11, pp. 2490-2494, 2011.

[17] S. Bowden &. C. Honsberg, “PVeducation.org - PVCDROM,” 2012. [Online]. Available: http://www.pveducation.org/pvcdrom/. [Accessed 28 May 2012].

[18] M. Dresselhaus et al., “Nanowires,” in *Springer Handbook of Nanotechnology*, Springer, 2010, pp. 119-167.

[19] R. Wagner &. W. Ellis, “Vapor-Liquid-Solid Mechanism of Single Crystal Growth,” *Applied Physics Letters,* vol. 4, no. 5, pp. 89-90, 1964.

[20] A. Persson et al., “Growth mechanisms for GaAs nanowires grown in CBE,” *Journal of Crystal Growth,* vol. 272, pp. 167-174, 2004.

[21] K. Dick et al., “Failure of the Vapor-Liquid-Solid Mechanism in Au-Assisted MOVPE Growth of InAs Nanowires,” *NANO Letters,* vol. 5, no. 4, pp. 761-764, 2005.

[22] K. Dick et al., “A New Understanding of Au-Assisted Growth of III-V Semiconductor Nanowires,” *Advanced Functional Materials,* vol. 15, pp. 1603-1610, 2005.

[23] J. Johansson et al., “Growth related aspects of epitaxial nanowires,” *Nanotechnology,* vol. 17, pp. 355-361, 2006.

[24] B. Tian et al., “Coaxial silicon nanowires as solar cells and nanoelectronic power sources,” *nature,* vol. 449, pp. 885-890, 2007.

[25] B. Tian et al., “Single nanowire photovoltaics,” *Chemical Society Review,* vol. 38, no. 1, pp. 16-24, 2009.

[26] M. Putnam et al., “Si Microwire-Array Solar Cells,” *Energy & Environmental Science,* vol. 3, no. 8, pp. 1037-1041, 2010.

[27] H. Goto et al., “Growth of Core–Shell InP Nanowires for Photovoltaic Application by Selective-Area Metal Organic Vapor Phase Epitaxy,” *Applied Physics Express,* vol. 2, no. 035004, pp. 1-3, 2009.

[28] E. Garnett et al., “Nanowire Solar Cells,” Annual Reviews, Department of Materials Science, Stanford University, Stanford, 2011.

[29] H. Pettersson et al., “Electrical and optical properties of InP nanowire ensemble p+in+ photodetectors,” *Nanotechnology,* vol. 23, no. 135201, pp. 1-6, 2012.

[30] A. Pierret et al., “Generic nano-imprint process for fabrication of nanowire arrays,” *Nanotechnology,* vol. 21, pp. 1-6, 2010.

[31] Y. Ahn et al., “Photocurrent Imaging of p-n Junctions in ambipolar Carbon Nanotube Transistors,” *NANO Letters,* vol. 7, no. 11, pp. 3320-3323, 2007.

[32] N. Tajik et al., “Sulfur passivation and contact methods for GaAs nanowire solar cells,” *Nanotechnology,* vol. 22, pp. 1-7, 2011.

[33] A. Lysov et al., “Spatially Resolved Photoelectric Performance of Axial GaAs Nanowire pn-Diodes,” *Nano Research,* vol. 4, no. 10, pp. 987-995, 2011.

[34] B. Macht et al., “Patterns of efficiency and degradation in dye sensitization solar cells measured with imaging techniques,” *Solar Energy Materials & Solar Cells,* vol. 73, pp. 163-173, 2002.

[35] T. Jeranko et al., “Patterns of efficiency and degradation of composite polymer solar cells,” *Solar Energy Materials & Solar Cells,* vol. 83, pp. 247-262, 2004.

[36] C. McNeill et al., “Direct Photocurrent Mapping of Organic Solar Cells Using a Near-Field Scanning Optical Microscope,” *NANO Letters,* vol. 4, no. 2, pp. 219-223, 2004.

[37] T. Brenner & C. McNeill, “Spatially Resolved Spectroscopic Mapping of Photocurrent and Photoluminescence in Polymer Blend Photovoltaic Devices,” *The Journal of Physical Chemistry,* vol. 115, pp. 19364-19370, 2011.

[38] B. Leever et al., “Spatially resolved photocurrent mapping of operating organic photovoltaic devices using atomic force photovoltaic microscopy,” *Applied Physics Letters,* vol. 92, no. 013302, pp. 1-3, 2008.

[39] J. Hwang et al., “Photocurrent Mapping in High-Efficiency Radial p-n Junction Silicon Nanowire Solar Cells Using Atomic Force Microscopy,” *The Journal of Physical Chemistry,* vol. 115, pp. 21981-21986, 2011.

[40] M. Schwalm et al., “Characterization of solar cells by photocurrent spectroscopy and current-voltage characteristics with high spatial resolution,” *Optics Express,* vol. 18, no. 6, pp. 6277-6287, 2010.